

Dynamical properties of $z \sim 4.5$ dusty star-forming galaxies and their connection with local early type galaxies

Francesca Rizzo^{1,2,3, *}, Simona Vegetti¹, Filippo Fraternali⁴, Hannah R. Stacey¹, Devon Powell¹

¹Max-Planck Institute for Astrophysics, Karl-Schwarzschild Str. 1, D-85748, Garching, Germany

²Cosmic Dawn Center (DAWN), Denmark

³Niels Bohr Institute, University of Copenhagen, Lyngbyvej 2, DK-2100 Copenhagen Ø, Denmark

⁴University of Groningen, Kapteyn Astronomical Institute, Postbus 800, 9700 AV Groningen, The Netherlands

Accepted 2021 August 3. Received 2021 August 3; in original form 2021 February 10

ABSTRACT

There is a large consensus that gas in high- z galaxies is highly turbulent, because of a combination of stellar feedback processes and gravitational instabilities driven by mergers and gas accretion. In this paper, we present the analysis of a sample of five Dusty Star Forming Galaxies (DSFGs) at $4 \lesssim z \lesssim 5$. Taking advantage of the magnifying power of strong gravitational lensing, we quantified their kinematic and dynamical properties from ALMA observations of their [CII] emission line. We combined the dynamical measurements obtained for these galaxies with those obtained from previous studies to build the largest sample of $z \sim 4.5$ galaxies with high-quality data and sub-kpc spatial resolutions, so far. We found that all galaxies in the sample are dynamically cold, with rotation-to-random motion ratios, V/σ , between 7 to 15. The relation between their velocity dispersions and their star-formation rates indicates that stellar feedback is sufficient to sustain the turbulence within these galaxies and no further mechanisms are needed. In addition, we performed a rotation curve decomposition to infer the relative contribution of the baryonic (gas, stars) and dark matter components to the total gravitational potentials. This analysis allowed us to compare the structural properties of the studied DSFGs with those of their descendants, the local early type galaxies. In particular, we found that five out of six galaxies of the sample show the dynamical signature of a bulge, indicating that the spheroidal component is already in place at $z \sim 4.5$.

Key words: galaxies: evolution – galaxies: high-redshift – galaxies: ISM – galaxies: kinematics and dynamics – submillimetre: galaxies – gravitational lensing: strong

1 INTRODUCTION

Within the framework of current galaxy formation and evolutionary models, galaxies grow by acquiring material through gas accretion and mergers (e.g., Dekel et al. 2009; Rodriguez-Gomez et al. 2016; Naab & Ostriker 2017). Feedback processes driven by active galactic nuclei (AGN) or star formation are able to temper the growth of galaxies through the heating or expulsion of gas (Hopkins et al. 2012; Silk 2013; Nelson et al. 2019a). On the other hand, many of these feedback processes operate on physical scales that are well below the resolution of current cosmological simulations, and are, therefore, usually parametrized using simple sub-grid prescriptions which are mostly calibrated to match observations in the local Universe (e.g., Crain et al. 2015; Kim & Ostriker 2018; Vogelsberger et al. 2020).

Observational evidence able to give a consistent and quantitative picture of how galaxies grow and evolve across cosmic time is still lacking. For example, the importance of mergers in driving the stel-

lar mass growth, as well as in determining the resulting kinematic and chemical properties of galaxies, is still a matter of debate (e.g. Oesch et al. 2010; Satyapal et al. 2014; Eliche-Moral et al. 2018). The influence of feedback processes (e.g., outflows, turbulence), mergers and gas accretion in regulating the growth of stellar mass is observationally challenging to evaluate, even in the local Universe, since complex physical mechanisms operating at different scales need to be identified and constrained (e.g., Ciccone et al. 2016; Concas et al. 2017; McQuinn et al. 2019). Moreover, at high redshift, these challenges are exacerbated due to the limited angular resolution and signal-to-noise ratio (SNR) of the current observations (e.g., Chisholm et al. 2017; Stanley et al. 2019; Ginolfi et al. 2020). One of the ways to partly overcome these observational limitations is to target strongly gravitationally lensed galaxies. The magnification provided by gravitational lensing increases the solid angle of background sources and hence their observed total flux (Schneider 2006). As a result, distant objects can be observed with either increased spatial resolution (for spatially-resolved observations) or increased SNR (for unresolved observations).

Recently, Rizzo et al. (2020) showed the power of high resolu-

* E-mail: francesca.rizzo@nbi.ku.dk

tion observations in unveiling the dynamical properties of a lensed dusty star-forming galaxy (DSFG), SPT0418-47, at $z = 4.2$. In particular, they found that SPT0418-47 has dynamical properties similar to those of local spiral galaxies: it is rotationally supported and has a low level of turbulence, that is, it is dynamically cold. These features indicate that, unexpectedly, the high star-formation rate (SFR) and the gas fraction measured for this DSFG do not drive high turbulent motions nor affect the stability of the galaxy. Fraternali et al. (2021) obtained a similar result for two non-lensed DSFGs at $z \approx 4.5$. The global SFR and interstellar medium (ISM) properties of these three galaxies are typical of the population of DSFGs (Hodge et al. 2015; Aravena et al. 2016; Gómez-Guijarro et al. 2018), suggesting that such systems are common among star-forming galaxies at high redshifts. However, reproducing the existence of galaxies with such a large rotational velocity, SFR and content of cold gas remains challenging for most numerical simulations and semi-analytic models (e.g. Dekel & Burkert 2014; Zolotov et al. 2015; Pillepich et al. 2019; Dekel et al. 2020). Robust observational constraints on the spatially-resolved kinematic properties of star-forming galaxies at $z \gtrsim 4$ are thus necessary to inform us about how galaxies build up their mass and how they are affected by different physical processes.

Hodge et al. (2012) obtained the first spatially-resolved kinematics of a galaxy at $z = 4$, GN20, using CO observations from the Very Large Array. However, the long integration times (e.g., ≈ 120 hours for GN20) needed to spatially resolve the faint CO transitions made very challenging the extension of this analysis to a large sample of $z \gtrsim 4$ galaxies. In the past six years, the advent of the Atacama Large Millimetre/Submillimetre Array (ALMA, Wooten & Thompson 2009) has opened up a new frontier for detailed kinematic studies of galaxies in the redshift range $z \sim 4 - 6$ using the ${}^2P_{3/2} \rightarrow {}^2P_{1/2}$ transition at 1900.5469 GHz (157.74 μm , [CII]) of the ionized carbon C+ (e.g., De Breuck et al. 2014; Jones et al. 2017; Smit et al. 2018; Neeleman et al. 2020; Rizzo et al. 2020; Fraternali et al. 2021). The 158 μm [CII] emission line is, in fact, a powerful tool to investigate the gas physical conditions in the distant Universe: it is typically the brightest fine-structure line emitted in star-forming galaxies, representing $\sim 0.1 - 1$ percent of the total far-infrared luminosity in the most active systems (Stacey et al. 2010a; Sargsyan et al. 2014).

By studying the structural properties of star-forming galaxies at $4 \lesssim z \lesssim 5$, we also gain insights into the formation of massive quiescent galaxies at lower redshift. Stellar population studies of local early type galaxies (ETGs) have shown, indeed, that more than half of the stars in the most massive galaxies were formed at $z \gtrsim 3$ (McDermid et al. 2015). Furthermore, recent studies have found a spectroscopically-confirmed population of massive, quiescent galaxies already at $3 \lesssim z \lesssim 4$ (Glazebrook et al. 2017; Tanaka et al. 2019; Valentino et al. 2020). The properties of the quiescent populations both at low and intermediate redshifts suggest that their progenitors should belong to the star-forming population at $z \gtrsim 3$ (McDermid et al. 2015; Belli et al. 2017; Hodge & da Cunha 2020). The matching number densities, stellar masses and sizes of the massive star-forming at $z \gtrsim 4$ and quiescent populations at lower redshifts seem to support this picture (Toft et al. 2012; Valentino et al. 2020). The common structural feature of these quiescent systems is the presence of a spheroidal component, i.e., a bulge (e.g., Krajnović et al. 2013; Lang et al. 2014; van der Wel et al. 2014; Belli et al. 2017; Lustig et al. 2020). Despite several theories and scenarios have been proposed (e.g. Elmegreen et al. 2008; Bournaud et al. 2009; Kormendy 2016; Erwin & Debattista 2017; Brooks & Christensen 2016), to this date, it is still unclear which are the main

mechanisms driving the rapid formation of these bulges already at these early times (e.g. Kormendy 2016; Dimauro et al. 2019; Nelson et al. 2019b; Tacchella et al. 2018). A robust measurement of the kinematic and structural properties of $4 \lesssim z \lesssim 5$ galaxies requires high spatial resolution observations, which nowadays can be achieved efficiently by targeting strongly gravitationally lensed galaxies with ALMA. In this paper, we extend the dynamical analysis of SPT0418-47 (Rizzo et al. 2020) to a sample of five lensed DSFGs. Using the 3D kinematic-lens modelling technique developed by Rizzo et al. (2018) and applied to ALMA interferometric data, we reconstruct the dust and [CII] emission in these galaxies on sub-kpc scales. In Section 2, we describe the targets, observations and data reduction process. In Section 3, we summarise our lens modelling and source reconstruction technique and the dynamical analysis on the background sources. In Sections 4 and 5, we present the results and discuss the implications of our findings. The main conclusions of this work are summarized in Section 6. Throughout the paper, we assume a Λ CDM cosmology, with Hubble constant $H_0 = 67.8$ km/s/Mpc, matter density $\Omega_m = 0.308$, and vacuum energy density $\Omega_\Lambda = 0.691$ from Planck Collaboration et al. (2016).

2 SAMPLE AND OBSERVATIONS

2.1 The 158- μm [C II] emission line: a tracer of the gas kinematics at high- z

The 158- μm [CII] emission line can trace multiple phases of the ISM, including the warm ionized, the warm and cold neutral atomic, and the dense molecular medium (Stacey et al. 2010b), due to the lower ionization potential of 11.3 eV of the atomic carbon with respect to HI. However, several studies (Rigopoulou et al. 2014; Cormier et al. 2015; De Breuck et al. 2019) found that more than 60 percent of the [CII] emission originates in the photodissociation regions, the external layers of molecular clouds heated by the far-ultraviolet photons emitted from OB stars. In these regions, both atomic and molecular hydrogen, as well as electrons, can collisionally excite the ground state of C+ ions producing the [CII] emission line. Furthermore, the molecular gas can be an efficient emitter of [CII] rather than CO (Pineda et al. 2013; Nordon & Sternberg 2016; Glover & Smith 2016). Specifically, in low-metallicity environments or the outer regions of molecular clouds, H_2 self-shields and survives while CO can be easily photodissociated into C and C+ (e.g., Papadopoulos et al. 2002; Wolfire et al. 2010; Madden et al. 2020). This wide range of physical conditions makes [CII] an excellent tracer of the kinematics of high- z star-forming galaxies over large areas of their discs.

2.2 Selection of the sample

The targets in this paper are five gravitationally lensed DSFGs (Table 1). We collect the sample by selecting from the ALMA public archive star-forming galaxies at $4 \lesssim z \lesssim 5$ which are lensed by a galaxy or a galaxy group and with data of angular ($\lesssim 0.3$ arcsec) and spectral ($\lesssim 40$ km/s) resolutions high enough to resolve the emission of the 158- μm [CII] emission line (Table 1). In addition, we select observations with a median (over the spectral channels) SNR of the order of 10. The modelling code that we will apply to these data requires, indeed, fairly high SNRs (Rizzo et al. 2018), since it fits the data in all spectral channels, without requiring any projections to first and second moment maps. This approach is fundamental to obtain robust kinematic measurements, not affected by

the so-called beam smearing effect, which may cause strong bias to low values of the rotation velocities and high values of the velocity dispersions (Di Teodoro & Fraternali 2015). Furthermore, these high SNRs guarantee that no spatial binning is required, so that we can fully take advantage of the angular resolution of ALMA and probe the kinematics of our sample on sub-kpc scales.

The five lensing system of our selected sample were identified in the South Pole Telescope (SPT) survey (Carlstrom et al. 2011; Vieira et al. 2010, 2013; Reuter et al. 2020) and have existing ancillary spectroscopic and imaging data in the sub-mm and far-infrared wavelength range, from which the redshifts of the background galaxies (Table 1) and the infrared luminosities (see Section 4.3) were derived (e.g., Weiß et al. 2013; Strandet et al. 2016; Reuter et al. 2020; Aravena et al. 2016).

2.3 ALMA data

The observations for each target have two spectral windows covering the redshifted rest frequency of the [CII] line and two spectral windows for the continuum. Each spectral window has 240 channels and a 1.875 GHz bandwidth. In this paper, we make use of the calibrated measurement sets provided by the European ALMA Regional Centre (Hatziminaoglou et al. 2015), that calibrated the raw visibility data using the ALMA pipeline in the CASA package (McMullin et al. 2007). These data were then inspected to confirm the quality of the pipeline calibration and that no further flagging was required. We then performed one or two rounds of phase-only self-calibration on the continuum data, using solution intervals of the scan length or half the scan length and applied the complex gain corrections from the continuum to the spectral windows containing the line. The continuum is subtracted from the line spectral window using UVCONTSUB. The data are averaged into groups of between four (e.g., SPT0345-47, SPT2132-58) and six (e.g., SPT0441-46, SPT2146-55) channels in order to increase the overall SNR. This procedure results in channels with a typical velocity width of ≈ 30 km s⁻¹ (see Table 1).

The targets are imaged with natural weighting of the visibilities and deconvolved using CLEAN (Högbom 1974). In the panels a to c of Fig. 1 and Figs. B1-B4 in Appendix B, we show the spectral line moment maps of the lensed galaxies. We note that these images are intended only for visualisation, as the analysis is performed on the visibility data directly (see Section 3).

3 ANALYSIS

In this section, we provide an overview of the lens-kinematic modelling technique with which we derive the [CII] surface brightness distribution in each spectral channel, as well as the kinematic and dynamical properties of the lensed galaxy. In addition, we also recover the surface brightness distribution of the sources from the continuum dataset.

To infer the lens mass models, the sources and their kinematic properties, we make use of the Bayesian pixellated technique developed by Rizzo et al. (2018) and further extended to the visibility domain by Powell et al. (2020). We refer the readers to the above papers for a detailed description of the methodology. Here, we provide a summary and emphasise that our modelling technique enables us to simultaneously reconstruct the lensing mass distribution (see Section 3.1) and the kinematics of the source (see Section 3.2) from the same three-dimensional (3D, two spatial and one spectral dimension) data, by fitting directly in their native

visibility plane. The dynamical analysis of the background galaxies is described in Section 3.3.

3.1 Lens mass modelling

We assume that the lens mass distribution is described by an elliptical power-law profile with an external shear component. The parameters defining the power-law profile are the surface mass density normalization κ_0 , the position angle θ , the axis ratio q and the slope γ . The lens mass model parameters define the projected mass density distribution, normalised to the critical density, as follows

$$\kappa(x, y) = \frac{\kappa_0 \left(2 - \frac{\gamma}{2}\right) q^{\gamma - \frac{3}{2}}}{2 \left[q^2 \left(x^2 + r_c^2 \right) + y^2 \right]^{\frac{\gamma-1}{2}}}. \quad (1)$$

The parameters defining the shear component are its strength Γ_{sh} and position angle θ_{sh} .

3.2 Source reconstruction and kinematic properties

In our methodology, the source is pixellated, that is, its surface brightness distribution is reconstructed on a grid that is adaptive to the varying resolution given by the local lensing magnification (Vegetti & Koopmans 2009). For the sample studied in this paper, the minimum spatial resolutions range from ≈ 20 to 130 pc and the median spatial resolutions range from ≈ 170 to 300 pc (see Appendix B1 for further details).

The kinematic-lens modelling technique adopted in this paper (Rizzo et al. 2018) makes use of a 3D kinematic model, that describes a rotating disc, as a regularising hyperprior to the pixellated source reconstruction. The kinematic model is defined by the geometrical parameters (inclination i and position angle PA) and the parameters describing the rotation and velocity dispersion curves. In particular, for all but one of the sources in the sample, we adopted a multi-parameter function (Rix et al. 1997) for their rotation curve

$$V_{\text{rot}}(R) = V_t \frac{\left(1 + \frac{R_t}{R}\right)^\beta}{\left[1 + \left(\frac{R_t}{R}\right)^\xi\right]^{1/\xi}}, \quad (2)$$

since it is flexible enough to reproduce a large variety of rotation curves (Rizzo et al. 2018). In contrast, we found that for SPT2132-58 a simpler arctangent function (e.g., Swinbank et al. 2011; Harrison et al. 2017; Turner et al. 2017),

$$V_{\text{rot}}(R) = \frac{2}{\pi} V_t \arctan\left(\frac{R}{R_t}\right), \quad (3)$$

was sufficient to fit the data to the noise level (see Section 4.1). We believe this to be related to the small Einstein ring ≈ 0.3 arcsec of this system that results in a lower spatial resolution and therefore in fewer available constraints.

Measurements of the cold gas velocity dispersion in nearby and high- z galaxies show that for most galaxies the values of σ decrease with increasing galactocentric radius, following an exponential or a linear trend (e.g., Tamburro et al. 2009; Mogotsi et al. 2016; Bacchini et al. 2019; Sharda et al. 2019; Lelli et al. 2021; Bacchini et al. 2020). For all of the galaxies in the sample, we assume the velocity dispersion curve to have an exponential profile

$$\sigma(R) = \sigma_0 e^{-\frac{R}{R_\sigma}}. \quad (4)$$

Table 1. Summary of the observed targets. Columns one and two: IAU and short name. Column three: lens redshifts from [Spilker et al. \(2016\)](#), when available. Column four: source redshifts from [Reuter et al. \(2020\)](#). Column five: total on-source integration times. Column six: ALMA project codes (PI: K. Litke). Column seven: beam size of the [CII] observations. Column eight: channel width of the [CII] data cube.

IAU Name	Short Name	z_{lens}	z_{source}	t_s min	Project code	Beam size arcsec \times arcsec	Channel width km s $^{-1}$
SPT-S J011308-4617.7	SPT0113-46	–	4.23	13.9	2016.1.01499.S	0.35×0.19	32.2
SPT-S J034510-4725.7	SPT0345-47	0.36	4.29	29.2	2016.1.01499.S	0.18×0.16	26.1
SPT-S J044143-4605.5	SPT0441-46	0.88	4.48	28.0	2016.1.01499.S	0.23×0.19	40.5
SPT-S J214654-5507.9	SPT2146-55	–	4.57	23.8	2016.1.01499.S	0.23×0.20	41.1
SPT-S J213244-5803.1	SPT2132-58	–	4.77	24.4	2016.1.01499.S	0.25×0.22	28.4

3.2.1 Modelling strategy

To infer the lens and kinematic parameters, and the source we apply an optimisation scheme, which is divided in the following stages:

(i) To find an initial guess for the lens parameters, we start by modelling the zeroth-moment map of the data.

(ii) We then model the 3D data cube and reoptimize for the lens parameters, starting from the values found in step (i). At this stage, the source is reconstructed on a pixellated grid, without the kinematic hyperprior.

(iii) We fix the lens parameters to the values found in step (ii) and we activate the source hyperprior, optimizing for the kinematic parameters. We check that the reconstructed source obtained at this stage is consistent with that obtained at point (ii). In Appendix A, Figs. A2 and A3, we show an example of the reconstruction of a lensed source which is not well described by a rotating disc.

3.3 Rotation curve decomposition

To quantify how the different matter components contribute to the total galactic gravitational potential of the source galaxies, we perform a rotation curve decomposition, similarly to what has been done in [Rizzo et al. \(2020\)](#). The rotation velocity $V_{\text{rot}}(R)$ of the gas is, indeed, related to the total gravitation potential of the galaxy Φ^1 by

$$R \left(\frac{\partial \Phi}{\partial R} \right)_{z=0} = V_c^2 = V_{\text{rot}}^2 + V_A^2, \quad (5)$$

where V_c is the circular velocity, and V_A is the asymmetric-drift correction that accounts for the pressure support due to the random motions (see equation 6 in [Rizzo et al. 2020](#)). To derive V_A not only the velocity dispersion profile $\sigma(R)$ is needed, but also the spatial distribution of the gas component, traced by the [CII] emission line. To this end, we assume that the gas has a spatial distribution described by an exponential profile,

$$\Sigma_{\text{gas}} = \Sigma_0 \exp\left(-\frac{R}{R_{\text{gas}}}\right). \quad (6)$$

To measure the scale radius R_{gas} , we divide the zeroth-moment map of the reconstructed sources (Fig. 1 and Figs. B1 to B4, panel d) in rings with centers, PA and i defined by the values of the kinematic models. We then azimuthally average the values inside each ring to obtain the surface density profile that is then fitted with

the exponential profile (Fig. C1).

We model the circular velocity as

$$V_c = \sqrt{V_{\text{star}}^2 + V_{\text{gas}}^2 + V_{\text{DM}}^2}, \quad (7)$$

where V_{star} , V_{gas} , V_{DM} are the contributions of the stellar, gas and dark matter components to the circular speed for which we make the following assumptions:

- the stellar component is described by a Sérsic profile ([Lima Neto et al. 1999](#); [Terzić & Graham 2005](#)). V_{star} is, therefore,

$$V_{\text{star}} = \sqrt{\frac{GM_{\text{star}}}{R} \frac{\gamma(n(3-p), b(R/R_e)^{1/n})}{\Gamma(n(3-p))}} \quad (8)$$

where M_{star} is the total stellar mass, R_e is the effective radius and n is the Sérsic index. In equation (8), γ and Γ are the incomplete and complete gamma function, respectively, while the parameters p and b are functions of the Sérsic index n (see Section 2 in [Terzić & Graham 2005](#)). The lack of spatially resolved data from the rest-frame optical or near-infrared emission prevents the fitting of two stellar components (i.e., bulge and disc), due to the strong degeneracies between the two. The single Sérsic component employed in the dynamical fitting should be, therefore, considered as a global description of the stellar distribution.

- The gas component has the same distribution as the [CII] emission line and it is defined by an exponential profile so that

$$V_{\text{gas}} = \sqrt{\frac{2GM_{\text{gas}}}{R_{\text{gas}}} y^2 [I_0(y)K_0(y) - I_1(y)K_1(y)]} \quad (9)$$

where $y = R/R_{\text{gas}}$ and K_0, K_1, I_0, I_1 are the modified Bessel functions ([Binney & Tremaine 2008](#)). Since the scale length R_{gas} is fixed at the value found above, the only free parameter of the fit for V_{gas} is the conversion factor ($\alpha_{[\text{CII}]}$) between the total [CII] luminosity and the total gas mass, $M_{\text{gas}} = \alpha_{[\text{CII}]} L_{[\text{CII}]}$ (see [Rizzo et al. 2020](#), and Appendix C for further details).

- With the current data, we can probe only the inner regions of our galaxy sample, mostly dominated by the baryonic components. However, for self-consistency, we make simple but reasonable assumptions for taking into account the dark matter contribution to the gravitational potential. The dark matter halo is modelled as a Navarro-Frenk-White (NFW [Navarro et al. 1996](#)) spherical halo,

$$V_{\text{DM}} = \sqrt{\frac{GM_{\text{DM}}}{R_{\text{DM}}} \frac{\ln(1+cx) - cx/(1+cx)}{x[\ln(1+c) - c/(1+c)]}}, \quad (10)$$

where c is the concentration parameters and M_{DM} and R_{DM} are

¹ This relation is obtained under the assumption that Φ is axisymmetric

the virial mass and radius, respectively. To reduce the number of free parameters, we fixed the value of c to the value obtained by averaging the values of the concentration parameters for dark matter halo masses in the mass range between $10^{10}M_{\odot}$ and $10^{13}M_{\odot}$ and assuming the mass-concentration relation estimated in N-body cosmological simulations (Dutton & Macciò 2014, see Table C1). We notice that at these redshifts, the concentration is almost independent of the dark-matter halo mass varying by at most 8 percent for a variation of 3 orders of magnitude in the halo mass (see Rizzo et al. 2020, for further details on this assumption). The only free parameter of V_{DM} is the virial mass M_{DM} , since the virial radius R_{DM} can be expressed as a function of M_{DM} .

To fit the circular velocities and compute the Bayesian posterior distribution of the free parameters (M_{star} , R_e , n , $\alpha_{[\text{CII}]}$, M_{DM}) we use DYNesty, a python implementation of the Dynamic Nested Sampling algorithm (Speagle 2019). We use flat prior distributions for R_e , n and $\alpha_{[\text{CII}]}$ and log-uniform priors for the mass parameters (see Table C2 in Appendix C).

4 RESULTS

The results of this lens-kinematic analysis can be visualised in three sets of figures for each lensed system. The first set shows the zeroth-, first- and second-moment maps of the data, the reconstructed source and the source kinematic model (Fig. 1 and Figs. B1 to B4). The second set displays the data, the model, the reconstructed source and the kinematic model for some representative channel maps (Fig. 2 and Figs. B5 to B8). In the source columns, we show the sources obtained with (gray solid contours) and without (dashed black contours) the kinematic hyperprior (see point (iii) in 3.2.1.) The third set of images shows the position-velocity (p-v) diagrams along the major and minor axis for the reconstructed sources (black contours) and their kinematic models (red contours, see Fig. 3 and Figs. B9 to B12). The most probable a posteriori lens and kinematic parameters are listed in Tables 2 and 3, respectively.

We note that four out of the five sources are lensed by a galaxy, while SPT0113-46 is lensed by a group of galaxies (Spilker et al. 2016). When modelling SPT0113-46, we therefore also included the contribution to the lensing potential of the three closest galaxies in the form of three elliptical power-law components. We found that this was sufficient to fit the data to the noise level (see column three in Fig. 2). The lens mass parameters listed in Table 2 are consistent with previous analysis of the same systems (Spilker et al. 2016). To define the lowest contours in Figs. 2 and 3 and the corresponding figures for the rest of the sample (Appendix B), we construct maps of the SNRs in each channel of the reconstructed source and define as reliable the pixels with $\text{SNR} \gtrsim 3$, allowing us to discriminate features in the reconstructed source from noise artefacts. The characterization of the noise in the source plane is not trivial: correlated noise features in the lens plane may be absorbed into the source reconstruction (Stacey et al. 2020). In particular, for the data sets used in our analysis, the uncertainties in the source surface brightness resulting from noise artefacts are, indeed, significantly larger than the uncertainties due to the lens model parameters. To estimate the uncertainties in the source plane, we, therefore, assume our maximum a posteriori source model and create mock lensed data with 100 different Gaussian realisations of the noise at the level measured in the real data. We then reconstruct the source from the mock data sets and measure the mean and standard deviation of

the surface brightness in each pixel and in each spectral channel.

4.1 Is a rotating disc a good model for galaxies at $z \sim 4.5$?

Both the figures containing the channels maps (Fig. 2 and Figs. B5 to B8) and the p-v diagrams (Fig. 3 and Figs. B9 to B12) show how well the rotating disc model is able to reproduce the emission of the reconstructed sources in our samples. The p-v diagrams along the major axis of the reconstructed sources (black contours) have, in fact, an S-shape, that is a typical signature of a rotating disc (see the red contours). The thickness of the p-v diagrams both along the major- and minor-axis is the result of the velocity dispersion and the instrumental resolution. At the central channel maps, close to the systemic velocity, the black contours of all galaxies have a "butterfly" shape, a typical pattern of a rotating disc.

We note also that on top of the bulk rotation motions two galaxies of the sample, SPT0441-46 and SPT2146-55, have anomalous kinematic components, features very common in nearby spiral galaxies (Fraternali et al. 2001, 2002). In particular, SPT0441-46 and SPT2146-55 show faint emission in the so-called forbidden regions (i.e., forbidden for rotation) of the p-v diagrams (see the black contours in the lower left quadrants in Fig. B10 and B11). These features are due to lag in rotation and non-circular motions and they are usually ascribed to extraplanar gas, bars or lopsided structures (Fraternali & Binney 2006; Sancisi et al. 2008). The inspection of the p-v diagrams and channel maps indicates that the derived kinematic parameters are robust also for these two galaxies. Due to the faint emission of the anomalous kinematic components, the kinematic models are, in fact, not influenced at all by them and are able to well reproduce the bulk of the gas in regular rotation. We also note that the presence of non-circular motions was suggested by Hodge et al. (2019) for a sample of DSFGs to explain the signatures of bars and non-axisymmetric structures not described by a smooth exponential brightness profile.

Rotating discs have been previously observed among the DSFG population at these redshifts (e.g., Hodge et al. 2012; Carniani et al. 2013; Tadaki et al. 2018; Sharda et al. 2019; Rizzo et al. 2020; Fraternali et al. 2021; Lelli et al. 2021). However, the presence of rotation is not sufficient to rule out the merger scenario as one of the main formation channels of the DSFG population. A number of numerical simulations showed that at high- z rotating gas discs can reform after gas-rich mergers (e.g., Robertson et al. 2006; Hopkins et al. 2013; Kohandel et al. 2020). We note also that mergers are not the unique processes that can explain the physical properties of DSFGs. For instance, using numerical and semi-analytical models, recent studies (e.g., Narayanan et al. 2015; Lacey et al. 2016; McAlpine et al. 2019; Lagos et al. 2020) showed how gas accretion, disc or bar instabilities can trigger the starburst phase and explain most properties of the DSFG population.

4.2 Dynamical properties

The rotation curves of the galaxies of our sample resemble those found for local spiral galaxies (Lelli et al. 2016). All rotation curves flatten, in fact, at large radii and show a variety of shapes in the inner regions. In particular, we can distinguish three main classes:

- rotation curves that steeply rise and then decline before flattening out to the outermost measured value (SPT0113-46, SPT0441-46). These curves are typical of nearby massive spiral galaxies with stellar bulges (Cimatti et al. 2019);

Table 2. Mass model parameters of the gravitational lens galaxies. From left to right we list the mass density profile normalisation, position angle, axis ratio, slope, the external shear strength and its position angle.

Name	κ_0 arcsec	θ deg	q	γ	Γ_{sh}	θ_{sh} deg
SPT0113-46	1.20±0.02	91±2	0.72±0.02	1.99±0.02	0.0013±0.0002	14±2
	0.43±0.02	178±6	0.9±0.1	2.1±0.2		
	0.15±0.02	37±2	0.8±0.1	2.0±0.1		
SPT0345-47	0.36±0.05	128.0±0.3	0.71±0.04	1.9±0.2	-0.027±0.004	-6±1
SPT0441-46	0.63±0.05	82±2	0.61±0.07	2.0±0.2	0.00011±0.00001	37±5
SPT2146-55	0.89±0.07	106±15	0.95±0.01	2.0±0.1	0.0136±0.0007	-24±3
SPT2132-58	0.30±0.01	105±8	0.64±0.07	2.0±0.1	-0.0610±0.003	-11.4±0.8

Table 3. Kinematic parameters of the sources. The kinematic model is a rotating disc defined by the geometrical parameters (i and PA) and the parameters defining the rotation curve, equations (2), (3), and velocity dispersion profile, equation (4).

Name	i deg	PA deg	V_t km s ⁻¹	R_t kpc	β	ξ	σ_0 km s ⁻¹	R_σ kpc
SPT0113-46	70±1	240±3	352±8	0.020±0.004	0.79±0.09	2.3±0.2	145±12	1.5±0.2
SPT0345-47	53±5	303±6	200±25	0.68±0.09	1.2±0.1	2.8±0.3	123±13	2.2±0.3
SPT0441-46	57±8	10±2	293±7	0.17±0.02	1.1±0.1	2.9±0.3	151±23	0.68±0.09
SPT2146-55	47±5	302±6	176±18	0.34±0.03	0.68±0.05	2.1±0.3	76±10	2.0±0.3
SPT2132-58	52±7	65±8	219±22	0.48±0.03	.	.	50±7	2.6±0.3

- rotation curves with an inner slow rise and then a flattening (SPT2132-58), typical of present-day disc galaxies;
- rotation curves with an intermediate behaviour (SPT0345-47, SPT2146-55).

The variety of the stellar distributions in these DSFGs is, therefore, imprinted in their dynamics. In particular, we confirm a previous finding (Rizzo et al. 2020): some DSFGs at $z \approx 4$ show the typical signature of a bulge, that is, a bump in the inner regions of the rotation curve.

By performing the rotation curve decomposition described in Section 3.3, we derive the parameters describing the three matter components, mass, gas and dark matter for each galaxy in the sample (Table 4). The respective posterior distributions are shown in Fig. C2. Fig. 4 shows for each galaxy of the sample the circular velocity and the rotation curve decomposition.

A previous estimate of the stellar mass, based on spectral energy distribution (SED) fitting, for one galaxy of our sample (SPT2146-55) is already present in the literature (Ma et al. 2015). The reported value is $0.8^{+1.9}_{-0.6} 10^{11} M_\odot$ (Ma et al. 2015), which, given its large uncertainties, is consistent at 1.1- σ level with the value of $1.0^{+0.17}_{-0.13} 10^{10} M_\odot$ found in this work (see Table 4). By using the same methodology for the rotation curve decomposition, Rizzo et al. (2020) found a stellar mass for SPT0418-47 of $1.7^{+0.2}_{-0.1} 10^{10} M_\odot$, consistent with the value of $9.5 \pm 3 10^9 M_\odot$ derived from SED fitting (De Breuck et al. 2019). The agreement between the values of stellar masses derived with these two different and independent methods demonstrates the robustness of the values of M_{star} derived from rotation curve decomposition.

We note that the regions probed by the [CII] emission line are baryon dominated: the ratio between the stellar and gas component

to the total matter at the outermost radius ranges from 0.66 ± 0.02 (SPT0441-46) to 0.90 ± 0.03 (SPT0345-47). For three out of the five galaxies of our sample, global measurements of the stellar-to-halo mass ratios ($M_{\text{star}}/M_{\text{DM}}$) are in the range $\sim 10^{-2}$ - 10^{-3} , in agreement with theoretical expectations (e.g., Behroozi et al. 2019). SPT0345-47 and SPT2132-58 have, instead, a $M_{\text{star}}/M_{\text{DM}}$ of $0.12^{+0.2}_{-0.06}$ and $0.6^{+0.2}_{-0.3}$, respectively. While at low- z , rotation curve fitting provides strong observational constraints on the stellar-to-halo mass ratios (Posti et al. 2019), at high- z constraints on the shapes of the dark matter halo profiles are challenging (see discussion in Genzel et al. 2020). However, in the context of Λ CDM, one can rely on the predictions of cosmological simulations that consistently show that the contribution of dark matter within the inner regions of galaxies is subdominant respect to the baryonic components (e.g., Lovell et al. 2018; Teklu et al. 2018). We emphasize, therefore, that our results, valid within the Λ CDM framework, show that there are small degeneracies between the baryonic and dark matter components (Fig. C2).

In Table 5 we list other derived physical quantities, which are relevant to our discussion (see Section 5), as the gas fraction f_{gas} and the total baryonic mass M_{bar} . The inferred values of M_{gas} are in agreement, within the 2- σ uncertainties, with the values derived from the CO luminosities, dust masses (Aravena et al. 2016), and [CI] luminosities (Bothwell et al. 2017). A detailed comparison between these different gas tracers is beyond the scope of this paper and is left to a future detailed investigation. We note that the median inferred value of $\alpha_{[\text{CII}]} = 7^{+4}_{-1} M_\odot/L_\odot$ is a factor of ~ 4 smaller than the value of $30 M_\odot/L_\odot$ found for main-sequence galaxies by Zanella et al. (2018). An $\alpha_{[\text{CII}]}$ of $30 M_\odot/L_\odot$ is excluded by the rotation curves as the resulting V_{gas} (eq. 9) would be larger than the observed V_c . In addition, by assuming $\alpha_{[\text{CII}]} = 30 M_\odot/L_\odot$,

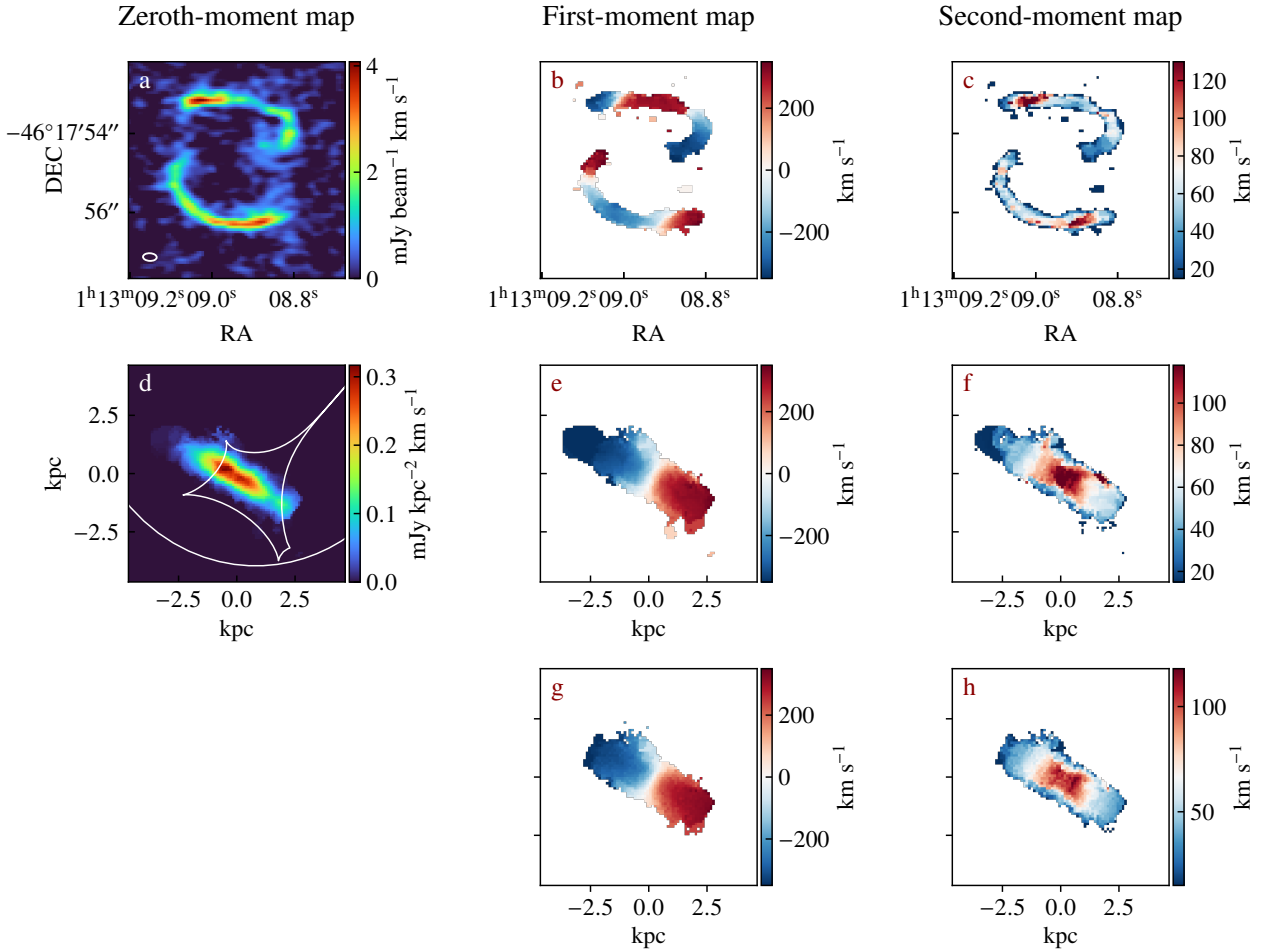


Figure 1. Moment maps for SPT0113-46. Panels a, b and c: the observed [CII] zeroth-, first- and second-moment maps. The beam size, shown as a white ellipse on the lower left corner of panel a, is 0.35×0.19 arcsec² at a position angle of 87.0° . Panels d, e and f: zeroth-, first- and second-moment maps of the reconstructed source. The white curves in panel d show the caustics. Panels g and h: first- and second-moment maps of the kinematic model. These maps are intended only for visualisation as the full analysis is performed on the data cube.

Table 4. Dynamical parameters of the sources. All parameters listed in columns two to six are inferred from the rotation curve decomposition assuming a Sérsic profile for the stellar component, an exponential profile for the gas disc and an NFW profile for the dark matter halo. From left to right: the stellar mass, the stellar distribution effective radius and Sérsic index, the conversion factor between the [CII] luminosities and the gas mass and the dark matter mass. Column 7 lists the best fit scale radii describing the [CII] profile.

Name	M_{star} $10^{10} M_{\odot}$	R_e kpc	n	$\alpha_{\text{[CII]}}$ M_{\odot}/L_{\odot}	M_{DM} $10^{11} M_{\odot}$	R_{gas} kpc
SPT0113-46	6^{+2}_{-1}	$1.4^{+0.6}_{-0.5}$	$6.0^{+0.5}_{-0.6}$	19^{+4}_{-3}	12^{+6}_{-6}	1.5 ± 0.2
SPT0345-47	$2.3^{+0.4}_{-0.3}$	$0.30^{+0.06}_{-0.04}$	$1.5^{+0.5}_{-0.3}$	7.3^{+1}_{-1}	2^{+2}_{-1}	0.76 ± 0.02
SPT0441-46	$1.8^{+0.2}_{-0.2}$	$0.11^{+0.02}_{-0.02}$	$2.0^{+0.9}_{-0.6}$	8^{+1}_{-1}	72^{+8}_{-8}	0.63 ± 0.07
SPT2146-55	$1.0^{+0.2}_{-0.1}$	$0.39^{+0.08}_{-0.05}$	$1.6^{+0.3}_{-0.2}$	$4.6^{+0.9}_{-0.8}$	$1.2^{+0.5}_{-0.5}$	1.4 ± 0.1
SPT2132-58	$1.9^{+0.3}_{-0.3}$	$1.4^{+0.1}_{-0.1}$	$0.94^{+0.05}_{-0.04}$	$7.2^{+0.9}_{-0.9}$	$0.32^{+0.23}_{-0.09}$	2.1 ± 0.2

the resulting values of M_{gas} would systematically overestimate the previous measurements from different gas tracers (Aravena et al. 2016; Bothwell et al. 2017). Values of $\alpha_{\text{[CII]}}$ of $10 M_{\odot}/L_{\odot}$ were previously assumed for DSFGs in the literature (e.g., Swinbank et al. 2012a; Gullberg et al. 2018), based on the comparison between CO(1-0) and [CII] luminosities (e.g., Stacey et al. 2010b; De Breuck

et al. 2011). Also, using theoretical prescriptions, Sommovigo et al. (2021) found that $\alpha_{\text{[CII]}}$ depends on the star-formation mode and it is typically $\lesssim 10 M_{\odot}/L_{\odot}$ in star-forming galaxies at $z \gtrsim 4$.

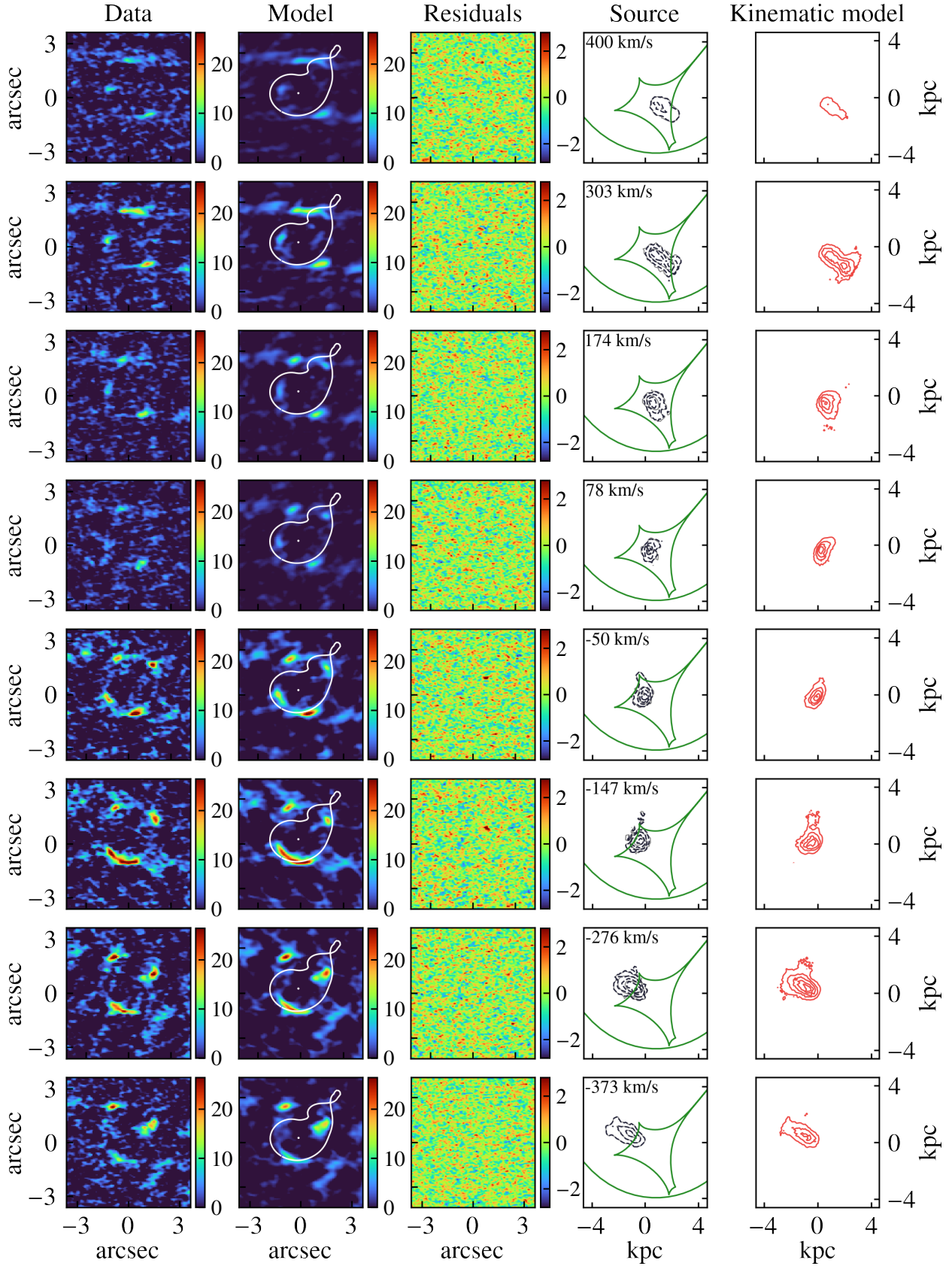


Figure 2. Representative channel maps for SPT0113-46 at the velocity shown on the upper left corner of column 4. Columns 1 and 2: dirty image of the data and the model. The colourbar units are mJy/beam. The white curves in the model columns show the critical curves. Column 3: dirty image residuals (data - model) normalized to the noise. Columns 4 and 5: reconstructed source and kinematic model with contours set at $n = [0.1, 0.3, 0.5, 0.7, 0.9]$ times the value of the maximum flux of the reconstructed source. In the source columns: the dashed black and solid gray contours show the sources obtained with and without a rotating disk as a hyperprior for the source reconstruction, respectively. The green curves in the source columns show the caustics.

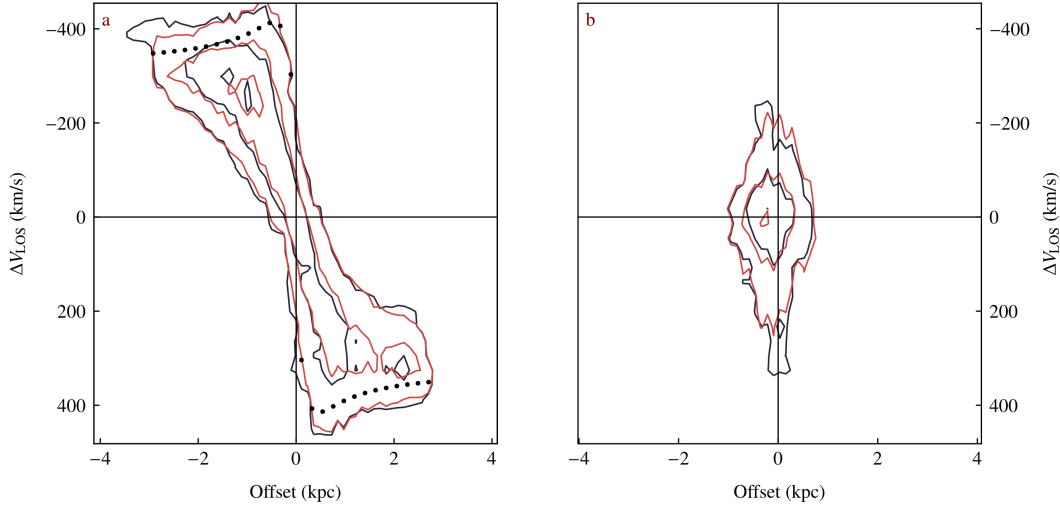


Figure 3. Position-velocity diagrams for SPT0113-46. The x-axes show the offset along the major (panel a) and minor axes (panel b) from the galaxy centre. The y-axis show the line-of-sight velocity centred at the systemic velocity of the galaxy. The reconstructed source is shown in black, the kinematic model in red. The black dots show the derived projected velocities.

Table 5. Derived physical properties of the sources. From left to right the gas mass, the fraction of total baryonic mass in gas, the total baryonic mass, the baryonic effective radius, the gas depletion time and the disc-scale height.

Name	M_{gas} $10^{10} M_{\odot}$	f_{gas}	M_{bar} $10^{10} M_{\odot}$	R_{bar} kpc	t_{dep} Myr	h pc
SPT0113-46	$4.3^{+1.0}_{-0.9}$	$0.39^{+0.11}_{-0.09}$	11^{+1}_{-1}	$2.2^{+0.4}_{-0.2}$	357 ± 73	100^{+86}_{-36}
SPT0345-47	$1.7^{+0.4}_{-0.4}$	$0.42^{+0.08}_{-0.09}$	$4.0^{+0.3}_{-0.3}$	$0.64^{+0.07}_{-0.05}$	12 ± 2	351^{+88}_{-88}
SPT0441-46	$1.4^{+0.2}_{-0.2}$	$0.45^{+0.05}_{-0.06}$	$3.2^{+0.2}_{-0.2}$	$0.35^{+0.06}_{-0.05}$	22 ± 4	225^{+105}_{-84}
SPT2146-55	$1.2^{+0.3}_{-0.2}$	$0.54^{+0.07}_{-0.08}$	$2.2^{+0.2}_{-0.2}$	$1.3^{+0.2}_{-0.2}$	17 ± 4	324^{+99}_{-73}
SPT2132-58	$1.9^{+0.3}_{-0.3}$	$0.50^{+0.07}_{-0.07}$	$3.9^{+0.4}_{-0.3}$	$2.5^{+0.1}_{-0.1}$	20 ± 4	368^{+90}_{-74}

4.3 Source continuum properties and SFR

In order to derive the star formation properties of the sources we model their continuum emission in a narrow spectral range close to the redshifted [CII] emission and use the strong lensing magnification factor (Table 6) to compute the intrinsic infrared luminosity from the observed values taken from the literature (Aravena et al. 2016, column two of Table 6). Specifically, these infrared luminosities were obtained from SED fitting of far-infrared and sub-millimeter observations, covering the range 250 to 3000 μm (Aravena et al. 2016). By applying the Kroupa Initial-Mass-Function (IMF) conversion factor of $1.48 \times 10^{-10} M_{\odot} \text{yr}^{-1} L_{\odot}^{-1}$ (Kennicutt & Evans 2012), we then derived the SFR for each source (column four of Table 6).

4.3.1 Position in the SFR - M_{star} plane

For most star-forming galaxies, there is a tight correlation between their SFR and their stellar mass (Brinchmann et al. 2004), the so-called main sequence. Several studies (e.g., Noeske et al. 2007; Whitaker et al. 2012; Steinhardt et al. 2014; Tasca et al. 2015) showed that the main sequence holds from $z = 0$ out to $z \sim 6$, with a redshift evolution of its normalization. Also, there are starburst galaxies, characterized by significantly higher SFR than normal main-sequence galaxies. While starburst galaxies are rare in the

Table 6. SFR and [CII] luminosities of the sources. Column two: the observed infrared luminosity from Aravena et al. (2016). Column three: the magnification factor of the continuum in the infrared bands. Column four: star-formation rate derived for a Kroupa IMF. Column five: intrinsic [CII] luminosities.

Name	$L_{\text{IR,obs}}$ $10^{13} L_{\odot}$	μ	SFR $10^2 M_{\odot} \text{yr}^{-1}$	$L_{[\text{CII}]}$ $10^9 L_{\odot}$
SPT0113-46	3.0 ± 0.5	36 ± 4	1.2 ± 0.3	2.3 ± 0.1
SPT0345-47	13 ± 2	14 ± 1	13 ± 3	2.3 ± 0.2
SPT0441-46	4.8 ± 0.9	10.8 ± 0.5	7 ± 1	1.8 ± 0.1
SPT2146-55	3.6 ± 0.8	7.8 ± 0.2	7 ± 1	2.6 ± 0.2
SPT2132-58	4.2 ± 0.7	6.3 ± 0.4	10 ± 2	3.7 ± 0.7

local Universe (Renzini et al. 2015), they constitute a moderate percentage (≈ 15 per cent, Bisigello et al. 2018; Caputi et al. 2017) of all galaxies at $z \gtrsim 2$, contributing up to 50 per cent of the cosmic SFR density at $z \sim 4$ (Caputi et al. 2017).

Starting from the physical properties derived in the previous section, we now explore the location of the source galaxies in the SFR - M_{star} diagram. We find that four out of five galaxies in our sample are consistent with the starburst sequence, while SPT0113-46 is a

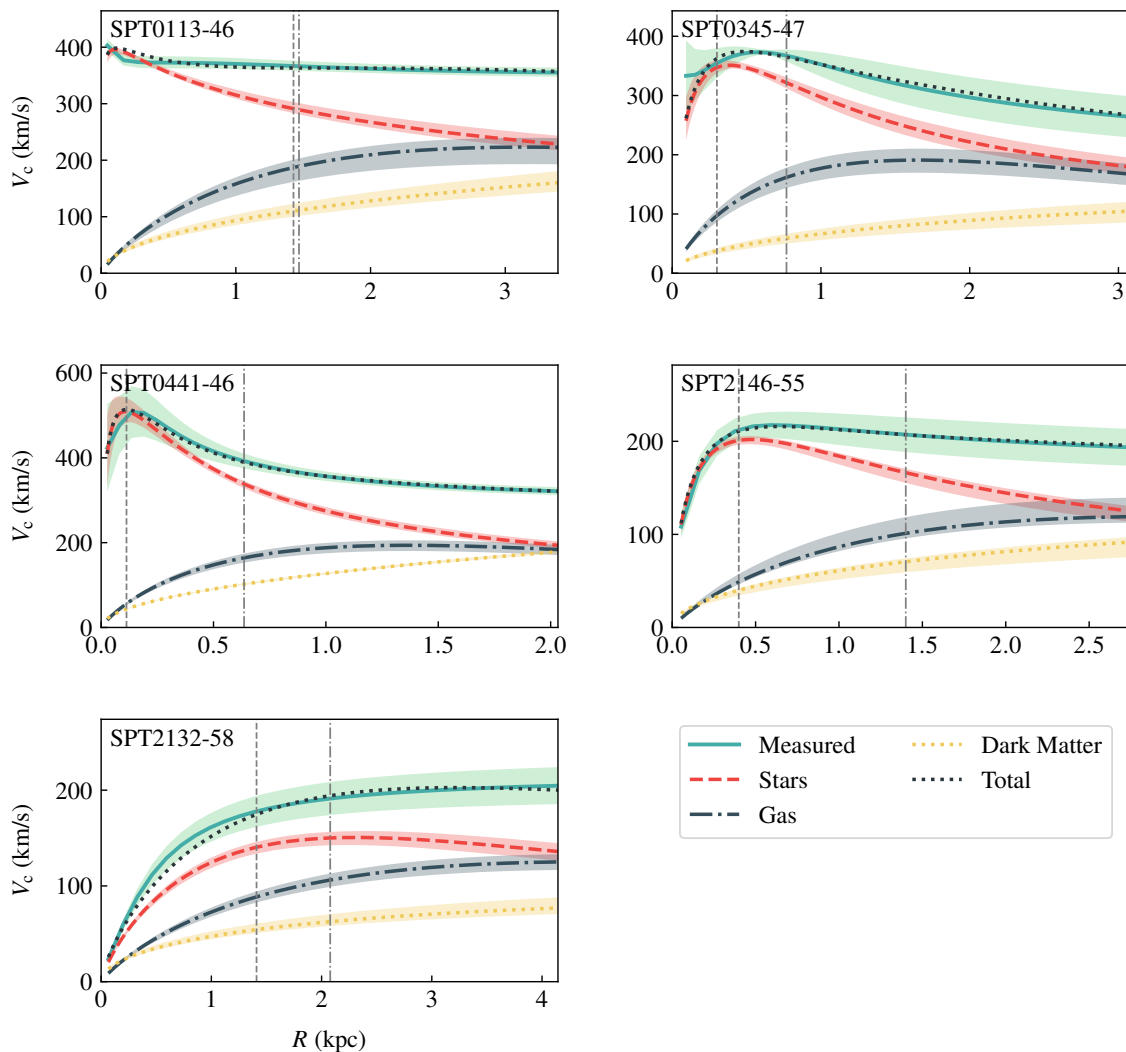


Figure 4. Rotation curve decomposition. The green solid lines show the circular velocity profiles. The black dotted lines show the best dynamical models, and the contribution from the different mass components as indicated by the legend and listed in Tables 4 and 5. The vertical gray dashed and dotted-dashed lines show the locations of R_e (effective radius of the stellar components) and R_{gas} (scale radius) of the gas component.

main-sequence galaxy. These findings are not surprising, given that the selection criteria used for the identification of the SPT DSFGs are based on the observed flux rather than the intrinsic one (Vieira et al. 2010, 2013). SPT0113-46 has, indeed, an observed infrared luminosity of $L_{\text{IR,obs}}$ which is similar to the rest of the sample (see column two in Table 6). However, the large magnification factor of ~ 36 leads to an intrinsic luminosity L_{IR} and SFR which are on average a factor of five below the other galaxies in the sample.

5 DISCUSSION

In this section, we investigate the dynamical and structural properties of the reconstructed sources. For the rest of this paper, we also include, if not otherwise stated, four non-lensed and one lensed DSFGs in our sample (see Table 7). These sources are the only $4 \lesssim z \lesssim 5$ DSFGs with beam-smearing corrected CO (Sharda et al. 2019) or [CII] kinematic measurements (Fraternali et al. 2021; Rizzo et al. 2020; Lelli et al. 2021) and without clear merging signatures.

5.1 V/σ ratio for non-merging DSFGs

Recent observational and theoretical studies (e.g., Swinbank et al. 2017; Wisnioski et al. 2015; Übler et al. 2019; Turner et al. 2017; Zolotov et al. 2015; Pillepich et al. 2019; Dekel et al. 2020) have suggested that many high- z galaxies, despite being rotationally supported systems, have intrinsic velocity dispersions which are much higher than those of local galaxies. The level of rotational support relative to the amount of turbulence in a galaxy is generally quantified with the ratio between the rotation velocity and the velocity dispersion, V/σ . We compute the V/σ ratios for our sample using two definitions: $V_{\text{max}}/\sigma_{\text{m}}$, the ratio between the maximum rotation velocity and the median velocity dispersion and $V_{\text{flat}}/\sigma_{\text{ext}}$, the ratio between the flat part of the rotation velocity and the velocity dispersion at outer radii (Table 8).

In Fig. 6, the $V_{\text{flat}}/\sigma_{\text{ext}}$ ratios are plotted as a function of redshift and compared with theoretical predictions (Pillepich et al. 2019; Dekel & Burkert 2014; Zolotov et al. 2015; Hayward & Hopkins 2017). We find that the ten galaxies of our extended sample have V/σ ratios which are systematically larger than any current theoret-

Table 7. Properties of the galaxies added to our sample. The kinematic properties in columns three to five are taken from the references shown in column six. The SFR value (converted to a Kroupa IMF) in column seven are taken from the references in column eight.

Name	z	V_{flat} km s $^{-1}$	σ_{ext} km s $^{-1}$	σ_{m} km s $^{-1}$	Reference	SFR M $_{\odot}$ yr $^{-1}$	Reference
SPT0418-47	4.23	259 \pm 1	18 \pm 1	32 \pm 1	Rizzo et al. (2020)	352 \pm 65	Rizzo et al. (2020)
AzTEC-1	4.34	200 \pm 27	30 \pm 8	40 $^{+20}_{-10}$	Sharda et al. (2019)	1261 $^{+38}_{-309}$	Tadaki et al. (2018)
J1000+0234	4.54	538 \pm 40	\leq 60	\leq 60	Fraternali et al. (2021)	468 $^{+1276}_{-340}$	Gómez-Guijarro et al. (2018)
AzTEC/C159	4.57	506 $^{+151}_{-76}$	16 \pm 13	16 \pm 13	Fraternali et al. (2021)	787 $^{+223}_{-180}$	Gómez-Guijarro et al. (2018)
ALESS073.1	4.75	309 $^{+47}_{-66}$	32 $^{+10}_{-9}$	47 $^{+15}_{-28}$	Lelli et al. (2021)	579 \pm 116	Circosta et al. (2019)

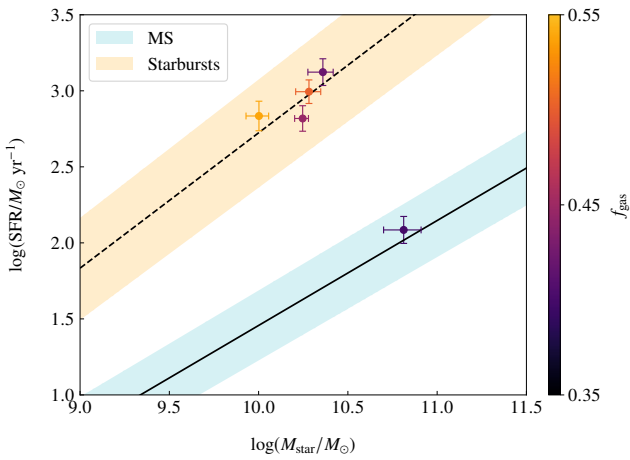


Figure 5. Location on the SFR - M_{star} of the source galaxies in our sample (circles), with markers colour-coded according to their gas fraction. The solid black line and the blue area show the best-fit and the 1- σ scatter for main-sequence galaxies at $z \sim 4 - 5$ from Caputi et al. (2017), respectively. The dotted black line and the orange area show the starburst sequence.

ical prediction. In particular, the median V/σ ratio of the sample is 11^{+4}_{-3} , which is a factor of 4 larger than the highest value of ≈ 3 predicted by TNG50 (Pillepich et al. 2019). This result confirms the findings presented in Rizzo et al. (2020), Fraternali et al. (2021) and Lelli et al. (2021) that DSFGs at these high redshifts may be significantly less turbulent than expected. However, we note that the velocity dispersions measured for the galaxies in our sample are typically higher than the thermal velocity dispersions of ≈ 10 km s $^{-1}$ expected for a gas at temperatures $T \lesssim 10^4$ K². These results imply a significant level of turbulence in the ISM of these galaxies, which is most plausibly (e.g. Übler et al. 2019; Krumholz et al. 2018; Varidel et al. 2020) related to either star-formation feedback (e.g., momentum injection by supernova explosions, stellar winds and expansion of HII regions) or gravitational phenomena (e.g., gas accretion, galaxy interactions and gravitational instabilities). Both

² The gas velocity dispersions, σ is the sum in quadrature of two contributions, $\sigma^2 = \sigma_{\text{th}}^2 + \sigma_{\text{turb}}^2$, where σ_{turb} is the velocity dispersion due to the turbulence and σ_{th} is the velocity dispersions due to the thermal motions of the particles within the gas (Cimatti et al. 2019). In particular, σ_{th} depends on the temperature T of the fluid: $\sigma_{\text{th}} = \sqrt{k_{\text{B}}T / (\bar{m}m_{\text{p}})}$, where k_{B} is the Boltzmann constant, \bar{m} is the mean average mass of the particle in the fluid in units of the proton mass, while m_{p} is the mass of the proton.

type of mechanisms may play an important role in driving turbulent motions also in nearby galaxies (see the discussion in Arribas et al. 2014; Bacchini et al. 2020; Varidel et al. 2020). Due to the high level of star-formation and the significant gas fraction, it is expected that both feedback and gravity-driven turbulence are more significant for high- z galaxies (Hung et al. 2019; Pillepich et al. 2019). In addition to the extended sample of DSFGs shown in Table 8, kinematic studies for two additional DSFGs can be found in the literature (Hodge et al. 2012; Carniani et al. 2013). For completeness, in Fig. 6, we plot the V/σ ratio including these objects. However, due to the potential bias affecting these measurements (see below), all quantitative consideration and discussion in this Section, are done including only kinematic measurements derived from 3D analysis. The derivation of the intrinsic values of V and σ requires to properly account for the beam using forward modelling techniques that fit the data in the native 3D space. However, some high- z dynamical analysis were performed on the projected velocity and velocity dispersion maps (2D analysis, e.g., Carniani et al. 2013; De Breuck et al. 2014). In this case, the velocity dispersions were beam-smearing corrected a posteriori by employing empirical relations (e.g., Swinbank et al. 2012b). Lelli et al. (2021) showed that the velocity dispersions obtained from an a-posteriori beam-smearing correction of the 2D maps are still biased to larger values: from a 2D study of the galaxy ALESS073.1, De Breuck et al. (2014) have inferred a value of σ which at outer regions is ~ 2 times larger than the one derived by Lelli et al. (2021) from a 3D analysis of the same galaxy³.

Another source of potential bias, is related to assumptions made on the velocity dispersion. For example, Tadaki et al. (2018, 2020) analyzed the CO(4-3) and [CII] kinematics of AzTEC-1 using a 3D technique (Bouché et al. 2015). In both cases, the authors assumed a constant velocity dispersion across the disk, finding a value of $\sigma \sim 74$ km s $^{-1}$ from the CO(4-3) and [CII] data. Relaxing this assumption, Sharda et al. (2019) found, instead, a strong decrease of the velocity dispersion with increasing galactocentric radius (from ~ 80 km s $^{-1}$ in the inner regions to ~ 30 km s $^{-1}$ at outer radii) by performing a 3D analysis of the same CO(4-3) data employed in Tadaki et al. (2018). The analysis in Sharda et al. (2019) demonstrated, therefore, that by fixing a constant velocity dispersion, one infers a value of σ which is mainly informed by the central regions of the galaxy. For consistency with our analysis (see Section 3.2), only the measurements from Sharda et al. (2019) are included in the extended sample and the discussion in the following sections.

³ In ALESS073.1, the velocity dispersions range from 10 to 40 km s $^{-1}$ in Lelli et al. (2021) and from 40 to 50 km s $^{-1}$ in De Breuck et al. (2014) at $R \gtrsim 2$ kpc, with average values of 22 km s $^{-1}$ and 40 km s $^{-1}$, respectively.

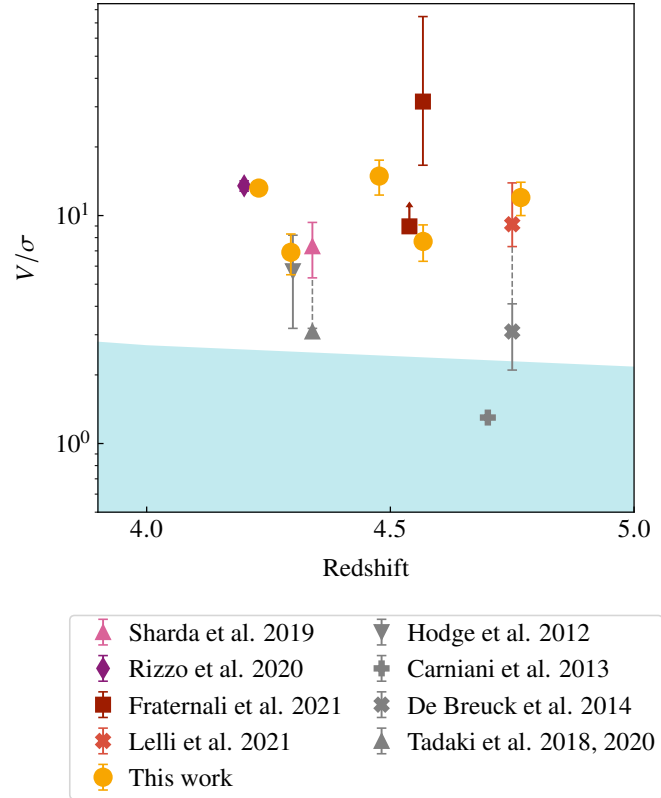


Figure 6. V/σ versus redshift. The V/σ for our sample (yellow circles), defined as $V_{\text{flat}}/\sigma_{\text{ext}}$ and for the non-merging DSFGs from literature (coloured markers, Table 7), as indicated in the legend. Note that the redshift of SPT0418-47 (orange diamond) is shifted by -0.02 for a better visualisation of all the points. The light-blue area shows the region covered by theoretical studies (Pillepich et al. 2019; Dekel & Burkert 2014; Zolotov et al. 2015; Hayward & Hopkins 2017). The gray markers show the V/σ measurements that may be affected by systematic bias (see Section 5.1). The dashed lines join the markers for which two different V/σ estimates for the same galaxy are available.

5.2 Drivers of turbulence in $z \sim 4$ non-merging DSFGs

We now compare our observations with an analytical model by Krumholz et al. (2018) that takes into account gravitational mechanisms, stellar feedback or both to describe the evolution of some observed properties of star-forming galaxies. For their models, Krumholz et al. (2018) assumed a rotating disc, made up of gas, stars and a spheroidal dark matter halo, in vertical hydrostatic and energy equilibrium. The dissipation of turbulence is counteracted by the injection of energy due to supernova explosions and the release of gravitational potential energy due to the inward flow of gas driven by non axisymmetric torques and gas accretion. The inclusion of either the two turbulence-driving mechanisms or only one of the two results in different relations between the velocity dispersions and the SFR. In the three panels in Fig. 7, we plot the σ -SFR relations obtained by assuming the fiducial parameters⁴ for the high- z galaxies shown in Table 3 of Krumholz et al. (2018), but with six different values of circular velocities matching those measured in our extended sample. The parameters defining the behaviour of σ

in these models are the Toomre parameter Q ⁵ and the star formation efficiency per free-fall time ϵ_{ff} :

- in the "Gravity + feedback" model (left panel in Fig. 7), the turbulence is driven by both stellar feedback and gravitational instabilities. The former are able to sustain the turbulence when $Q > 1$ (flat part of the curves at $\sigma \lesssim 25 \text{ km s}^{-1}$), while the latter play a key role for $Q = 1$. In this model, ϵ_{ff} is kept constant at 0.015. We note that the Toomre parameter for our sample has a median value of 1.1 , going from $0.7^{+0.4}_{-0.2}$ (SPT0441-46) to $1.5^{+0.2}_{-0.4}$ (SPT2146-55).

- The "Gravity" model (medium panel in Fig. 7) includes only the gravitational instabilities as drivers of turbulence within the model galaxies. The assumptions are similar to the "Gravity + feedback" model, except that Q is always equal to 1.

- The "Feedback, fixed ϵ_{ff} " (dashed lines in the right panel in Fig. 7) model is similar to the so-called 'self-regulated-system' model (Ostriker & Shetty 2011). In this case, the star formation is part of a self-regulating cycle where the momentum injected to the ISM by star formation balances the gravitational force confining the ISM gas in the disc, without any injection of gravitational potential energy. ϵ_{ff} is kept constant at 0.015 and Q is left free to vary.

⁴ A parameter defining the models by Krumholz et al. (2018) is the effective gas fraction at the mid-plane, $f_{\text{gas,P}} = 1.5 f_{\text{gas}}$ (Übler et al. 2019). In Fig. 7, we show the σ - SFR relations obtained by assuming the fiducial value $f_{\text{gas,P}} = 0.7$. However, we note that our results do not change by assuming values of $f_{\text{gas,P}}$ in the full range (0.6 - 0.8) probed by our sample.

⁵ The Toomre parameter considered in Krumholz et al. (2018) is defined as $Q = \frac{\Sigma_{\text{g}}}{\Sigma_{\text{g}} + [2\sigma^2 / (\sigma^2 + \sigma_{\text{star}}^2)] \Sigma_{\text{star}}} \frac{\kappa \sigma}{\pi G \Sigma_{\text{g}}}$, where Σ_{g} and Σ_{star} are the gas and stellar surface densities, σ_{star} is the stellar velocity dispersion and κ is the epicyclic frequency (Romeo & Falstad 2013).

• Also in the "Feedback, fixed Q " model (solid lines in the right panel in Fig. 7), stellar feedback is the only driving mechanisms of turbulence. Similarly to the model developed by [Faucher-Giguère et al. \(2013\)](#), the star-formation efficiency ϵ_{ff} is not constant and vary as a function of different properties of the galaxy, while $Q = 1$.

The comparison between the values of σ and SFR for the galaxies shown in Fig. 7 and these analytical models indicate that stellar feedback is able to sustain the measured turbulence (see the right panel in Fig. 7). The two models (left and medium panels) including gravitationally-driven mechanisms overestimate the velocity dispersions by factors from ≈ 7 (SPT0418-47) to ≈ 40 (SPT2132-58) for seven out of ten galaxies at the corresponding values of SFR. The only exceptions are SPT0113-46 that has a position consistent with all four models shown in Fig. 7 and J1000+0234 for which only an upper limit for the measured velocity dispersion is available ([Fraternali et al. 2021](#)). This result is at odds with recent works ([Krumholz et al. 2018](#); [Johnson et al. 2018](#); [Übler et al. 2019](#)) finding that gravitational instabilities are fundamental to explain the position of their galaxies in the σ -SFR plane with respect to the models of [Krumholz et al. \(2018\)](#). The reason for this discrepancy may be ascribed to the different galaxy populations and redshifts of the observed galaxies: starbursts at $z \sim 4.5$ in this paper, normal star-forming galaxies at $1 \lesssim z \lesssim 2$ in [Johnson et al. \(2018\)](#) and [Übler et al. \(2019\)](#) (see also discussion in Section 5.3). The major role of stellar feedback over other mechanisms in driving the observed properties of DSFGs at $z \sim 4 - 5$ was recently emphasized by [Spilker et al. \(2020\)](#).

5.2.1 Velocity dispersions and star-formation efficiencies

As a further test, in this section we estimate whether the velocity dispersions measured for our sample can be explained by the energy injected by supernova explosions using simple and reasonable assumptions. Following [Rizzo et al. \(2020\)](#) and [Fraternali et al. \(2021\)](#), the velocity dispersion due to the transferring of the supernova energy to the ISM is

$$\sigma_{\text{SFR}} = 58 \left(\frac{\epsilon_{\text{SN}}}{0.1} \frac{\text{SFR}}{300 M_{\odot} \text{yr}^{-1}} \frac{h}{200 \text{pc}} \right)^{1/3} \left(\frac{M_{\text{gas}}}{10^{10} M_{\odot}} \right)^{-1/3} \text{ km s}^{-1}, \quad (11)$$

where ϵ_{SN} is the efficiency of transferring kinetic energy from supernova feedback to the ISM and h is the disc scale height. Equation (11) is obtained by assuming a supernova rate of $0.01 M_{\odot}^{-1}$, valid for a Kroupa IMF ([Tamburro et al. 2009](#)). Since the calculation of the disc scale height is not trivial (see discussion in [Bacchini et al. 2019](#)), we use an analytical approximation and leave the exact estimate to a future work. The scale height of the vertical distribution of a gas disc in hydrostatic equilibrium can be approximated ([Bacchini et al. 2019](#)) as

$$h(R) = \frac{\sigma(R)}{\sqrt{4\pi G[\rho(R) + \rho_{\text{rot}}(R)]}} \quad (12)$$

with

$$\rho_{\text{rot}}(R) = -\frac{1}{2\pi G} \frac{V_{\text{c}}(R)}{R} \frac{\partial V_{\text{c}}(R)}{\partial R} \quad (13)$$

Since in this approximation, the self-gravity of the gas is not included, $\rho(R)$ is the density profile of the stellar and dark matter component and $\rho_{\text{rot}}(R)$ is obtained by considering equations (8) and (10).

The values of the median h for our sample are listed in column

seven of Table 5. In Fig. 8, we show the ratios between the expected values of σ_{SFR} and the measured σ_{m} (column three in Table 8). The σ_{SFR} values are calculated by using three values of ϵ_{SN} equal to 0.001, 0.01 and 0.1, typical of observed nearby ([Bacchini et al. 2020](#)) and simulated galaxies (e.g., [Martizzi et al. 2016](#); [Ohlin et al. 2019](#)). For all galaxies of our sample the ratios between σ_{m} and one of the three values of σ_{SFR} are ≈ 1 , confirming that the turbulent motions can be easily driven by supernova explosions (see Fig. 8). Larger values of ϵ_{SN} , 0.8-1, are, instead, considered an indication that other physical mechanisms, in addition to stellar feedback, drive the observed turbulent motions ([Utomo et al. 2019](#); [Tamburro et al. 2009](#)). We note that three galaxies in the sample (SPT0113-46, SPT0345-47, SPT0441-46) have values of velocity dispersions fully consistent with σ_{SFR} at $\epsilon_{\text{SN}} = 0.1$ within $1.5\text{-}\sigma$. For two galaxies (SPT2146-55, SPT2132-58), the σ_{SFR} values at $\epsilon_{\text{SN}} = 0.1$ overestimate σ_{m} by a factor of ≈ 3 , indicating that low efficiency values $0.01 \lesssim \epsilon_{\text{SN}} \lesssim 0.001$ are needed, similarly to what found both for high- and low- z star-forming galaxies ([Fraternali et al. 2021](#); [Bacchini et al. 2020](#)).

5.3 Turbulence across cosmic time

Our high-resolution 3D kinematic analysis shows that the sample of DSFGs studied in this paper has ratios of V/σ similar to those measured for spiral galaxies in the local Universe ([Lelli et al. 2016](#); [Bacchini et al. 2019](#)). The comparison with the intermediate- z star-forming galaxies is, instead, challenging, due to different gas tracers used in the literature to determine the evolution of the dynamical properties of galaxies across cosmic time. While it is firmly established that the kinematics of the molecular gas traces the galaxy kinematics, there is an open debate on the validity of this assumption for the ionized gas tracers at high redshift ([Girard et al. 2018](#); [Levy et al. 2018](#); [Lelli et al. 2018](#)). For example, by comparing the kinematics of the ionized ([OIII]) and neutral gas ([CI]) for a starburst galaxy at $z = 2.6$, [Lelli et al. \(2018\)](#) concluded that [OIII] traces the outflow motions, while [CI] is a tracer of the galaxy virial motions. On the other hand, [Übler et al. \(2018\)](#) found that the kinematics of the $\text{H}\alpha$ and CO(3-2) emission line are consistent in a star-forming galaxy at $z = 1.4$. The comparison between the dynamic properties of our DSFG sample with those found for intermediate- z galaxies from ionized gas tracers, reveals that the V/σ ratios of $z \sim 4.5$ galaxies are, on average, larger than V/σ measured from the ionized gas at lower redshifts. This difference may be ascribed to a combination of the following reasons:

- the samples of galaxies in the redshift ranges 1 to 2 with $\text{H}\alpha$ or [OII] measurements have typical rotation velocities $\lesssim 250 \text{ km s}^{-1}$ (e.g., [Di Teodoro & Fraternali 2015](#); [Swinbank et al. 2017](#); [Übler et al. 2017](#)). The DSFGs in our sample have V_{flat} from ≈ 200 to 360 km s^{-1} (see Table 8) and a median value of 280 km s^{-1} . The velocity dispersions σ_{ext} of our sample (from 16 to 40 km s^{-1} , see Table 8) are consistent with the distribution of the $\text{H}\alpha$ velocity dispersions of $z \approx 1$ star-forming galaxies found by [Di Teodoro & Fraternali \(2015\)](#) and [Übler et al. \(2019\)](#), but they overlap only with the low velocity-dispersion distribution at $z \gtrsim 1.5$ ([Übler et al. 2019](#)).

- The velocity dispersions measured from the ionized tracers is, on average, higher than those measured from the molecular and neutral media tracers both at low- ([Varidel et al. 2020](#); [Girard et al. 2021](#)) and high- z ([Girard et al. 2018](#)).

- The $\text{H}\alpha$, [OIII], and [OII] emission lines are not good tracers of the galaxy dynamics. A recent study ([Levy et al. 2018](#)) on a sample of local galaxies showed, for example, that the kinematics

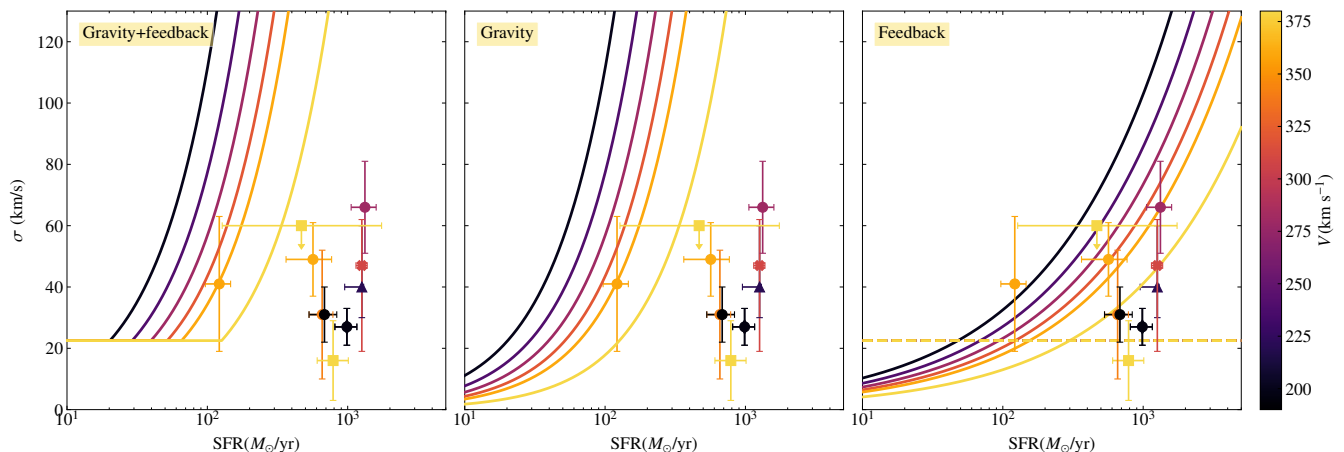


Figure 7. The markers show the σ_m (column three in Table 8) and SFR (column four in Table 6) for our sample (circles) and for the galaxies from Rizzo et al. (2020, diamond), Sharda et al. (2019, triangle), Fraternali et al. (2021, squares) and Lelli et al. (2021, cross). All markers are colour-coded according to V_{flat} (column five in Table 8 and column three in Table 7). In the four panels, the curves show the predictions of the relation between velocity dispersions and SFR in the analytic model developed by Krumholz et al. (2018), obtained with the parameters valid for high- z galaxies. The left and medium panels show the models that include gravitational instabilities plus stellar feedback and only gravitational mechanisms as the main drivers of turbulence within galaxies, respectively. The right panel shows models with only stellar feedback-driven turbulence: "Feedback, fixed Q " (solid lines) and "Feedback, fixed ϵ_{ff} " (dashed lines).

Table 8. Global kinematic parameters of the sources. Column two: the maximum rotation velocity. Column three: the median velocity dispersion. Column four: the ratio between V_{max} and σ_m . Column five: the rotation velocity in the flat part of the rotation curve. Column six: the velocity dispersion in the external regions ($R \geq R_e$). Column seven: the ratio between V_{flat} and σ_{ext} .

Name	V_{max}	σ_m	V_{max}/σ_m	V_{flat}	σ_{ext}	$V_{\text{flat}}/\sigma_{\text{ext}}$
SPT0113-46	382 ± 9	41 ± 22	9.2 ± 4.8	358 ± 3	27 ± 1	13.2 ± 0.6
SPT0345-47	373 ± 5	66 ± 15	5.6 ± 1.2	280 ± 25	40 ± 7	6.9 ± 1.4
SPT0441-46	489 ± 67	31 ± 21	15.8 ± 10.8	342 ± 4	23 ± 4	14.9 ± 2.6
SPT2146-55	217 ± 13	31 ± 11	7.0 ± 2.6	194 ± 7	20 ± 2	9.8 ± 1.2
SPT2132-58	199 ± 18	27 ± 6	7.2 ± 1.7	196 ± 14	16 ± 3	12 ± 2

of the molecular and ionized gas are different (Levy et al. 2018) and that the difference may be ascribed to stellar feedback processes. In particular, the measured ionized gas kinematics is affected by the presence of gas in outflows or in extraplanar layers. Unfortunately, the lack of good quality data of both the cold and warm gas for large samples of galaxies at $1 \lesssim z \lesssim 3$ prevents an accurate comparison between the kinematics of multiple phases of the ISM.

- The measured V/σ values can be biased towards low values due to some residual beam-smearing effect in some studies (see discussion in Di Teodoro & Fraternali 2015).

- The galaxies in our sample are starbursts (with the exception of SPT0113-46) while most of the galaxies with $H\alpha$ measurements at $1 \lesssim z \lesssim 2$ are main-sequence galaxies. The difference between these two galaxy populations should be taken into account before any detailed comparison of their dynamical properties. Furthermore, we do not expect an evolutionary connection between these two galaxy populations, that is, the starburst galaxies at $z \gtrsim 4$ are not the progenitors of the main-sequence galaxies at $z \lesssim 2$ (see Section 5.4 for further details).

We note, also, that the V/σ ratios measured for our DSFG sample are similar to those measured for the five galaxies of the comparison sample shown in Table 7 (see discussion in Section 5.1 for the

complete sample). We exclude that our results are affected by any specific assumption made to derive the kinematics of our sample (see Appendix A and Rizzo et al. 2018, for an extensive testing of the modelling technique used in this paper). We share, indeed, some methodologies and assumptions with previous works focusing on the kinematic study of high- z galaxies (e.g., Swinbank et al. 2017; Turner et al. 2017; Lelli et al. 2018; Übler et al. 2019; Wisnioski et al. 2019; Fraternali et al. 2021). We employ, indeed, a forward modelling approach similar to Di Teodoro et al. (2016), Lelli et al. (2018), Di Teodoro et al. (2018) and Fraternali et al. (2021). However, while they inferred model-independent velocities and velocity dispersions, we assume specific functional forms to describe the rotation velocity and velocity dispersion profiles, similarly to Swinbank et al. (2017), Turner et al. (2017) and Wisnioski et al. (2019). The comparison of the velocity dispersions of galaxies at different redshifts from similar tracers (i.e., HI, CO, [CII]) indicate that there is a weak decrease of the turbulence with time. The median value⁶ of $\approx 25 \text{ km s}^{-1}$ for the sample of $z \gtrsim 4$ DSFGs (markers with

⁶ The median σ of $25_{-9}^{+11} \text{ km s}^{-1}$ is obtained by including the upper limit of 60 km s^{-1} (Fraternali et al. 2021, red square in Fig. 9) as fiducial value. If this measurement is excluded, the resulting median σ is $25 \pm 7 \text{ km s}^{-1}$.

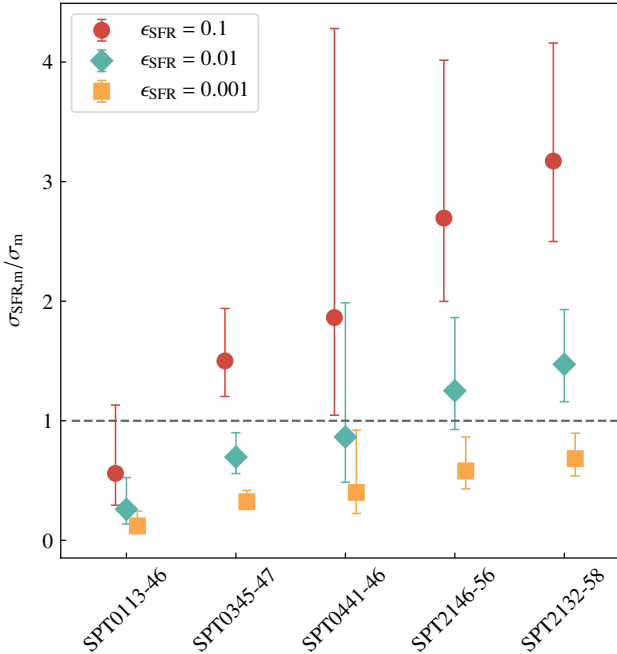


Figure 8. Ratio between the velocity dispersion expected from energy injection by the stellar feedback, equation (11), and the measured velocity dispersion σ_m (column three in Table 8). The three markers for each galaxy show the ratios obtained with three different values of ϵ_{SN} , as indicated in the legend.

errorbars in Fig. 9) is only a factor of ≈ 2 and 3 larger than the median HI σ ($12 \pm 2 \text{ km s}^{-1}$) and CO σ ($9^{+1}_{-2} \text{ km s}^{-1}$), measured in nearby galaxies (Bacchini et al. 2019, 2020). The comparison with the measurements from cold gas tracers (CO, [CI]) at intermediate- z indicates, instead, that the median σ at $z \gtrsim 4$ is similar to the median σ of $26^{+10}_{-7} \text{ km s}^{-1}$, measured for $1 \lesssim z \lesssim 3$ galaxies (Swinbank et al. 2011, 2015; Übler et al. 2019, 2018; Lelli et al. 2018; Girard et al. 2018). Larger samples of velocity dispersions from cold gas tracers at intermediate and high- z will be needed to confirm this trend and make a robust comparison between similar tracers and galaxy populations.

In Fig. 9, we also show the relations between velocity dispersions and redshifts derived by Übler et al. (2019) for main-sequence galaxies. In particular, the gray dotted and solid black lines are the best-fit relations for velocity dispersions measured from ionized ($\text{H}\alpha$, [OII], [OIII]) and atomic/molecular tracers (HI, CO) up to $z = 3.8$ and 2.4, respectively. The dash-dotted lines show, instead, the respective extrapolations up to $z \approx 6$. The comparison between the measured velocity dispersions at $z \gtrsim 3$ and the dash-dotted lines indicates that the extrapolated $\sigma - z$ relations are not valid at these high redshifts since they systematically overestimate σ by a median factor of ≈ 2 . We note, also, that this mismatch is even larger if we take into account that the $\sigma - z$ relations were derived mainly from normal star-forming galaxies, while both the galaxies in our sample and the four galaxies from the literature (Lelli et al. 2018; Sharda et al. 2019; Fraternali et al. 2021) are above the main-sequence and therefore more prone to develop high turbulent motions (e.g., Krumholz et al. 2018; Hung et al. 2019).

5.4 Evolutionary path: from DSFGs to ETGs

In this section, we compare the physical properties of the non-merging DSFGs with their plausible descendants, local ETGs. In particular, we focus on the position of these galaxies in the size-stellar mass plane ($R_e - M_{\text{star}}$). The relation between the size and stellar mass of galaxies, and how it evolves with cosmic time, provides, indeed, important insights onto the assembly history of galaxies (e.g., Hodge et al. 2016; van der Wel et al. 2014; Lang et al. 2014).

In Fig. 10 panels a and b, we show the position of our sample (circles) and SPT0418-47 (diamond) in the size-mass plane, colour-coded according to the gas fraction and depletion time ($M_{\text{gas}}/\text{SFR}$), respectively (see column six of Table 6). We note that we do not include the non-lensed galaxies listed in Table 7, as the few resolution elements across their discs do not allow a rotation curve decomposition similar to that performed for the lensed sample. In Fig. 10, we show also local ETGs (Cappellari et al. 2013) and high- z massive quiescent galaxies (Belli et al. 2017; Lustig et al. 2020; Esdaile et al. 2020; Kubo et al. 2018). The gray stars are $z \sim 2$ compact star-forming galaxies (cSFGs Barro et al. 2014). The cSFG have been proposed as a transition population between the star-forming and quiescent systems (e.g., Barro et al. 2014; van Dokkum et al. 2015). We note that for these comparison samples, only half-light radii are available in the literature, while the sizes derived from our rotation curve decomposition are the half-mass sizes. Systematic differences between these two measurements of size may arise from radial gradients in the mass-to-light ratios (e.g., Tortora et al. 2010; Mosleh et al. 2017; Suess et al. 2019a). For self-consistency, we therefore show in Fig. 10 the half-mass radii obtained after correcting the observed half-light radii with the relation by Suess et al. (2019a)⁷.

Interestingly, SPT0113-46, the only main-sequence galaxy in our sample (see Fig. 5), is consistent with the size-mass relation of local ETGs (panel a of Fig. 10). Its depletion time of ~ 357 Myr suggests that it can rapidly consume all of its gas and become a quiescent system. There is, indeed, growing evidence of the existence of a population of quiescent galaxies at $z \gtrsim 3$ (e.g., Glazebrook et al. 2017; Tanaka et al. 2019; Valentino et al. 2020). Moreover, three galaxies in our sample have Sérsic index $n \approx 1$, indicative of a discy stellar component, three other have $n \approx 2$, typical of discy bulges, while SPT0113-46 has the largest Sérsic index, $n \approx 6$. The Sérsic indices derived from our analysis suggest that the spheroidal components observed in $z \lesssim 3$ quiescent galaxies (Krajnović et al. 2013; Belli et al. 2017; Lustig et al. 2020) were already in place when the Universe was about 10 per cent of its current age.

In Fig. 10 panel b, we show how the stellar mass and size of the

⁷ The half-light radii of the local ETGs are rescaled by a factor of 0.7 (Suess et al. 2019b). For the high- z star-forming and quiescent galaxies at $z \sim 1 - 2$ (Barro et al. 2014; Belli et al. 2017; Lustig et al. 2020), the half-mass radii where obtained by multiplying the observed half-light ratio by the ratio r , such that $\log r = a[\log M_{\text{star}} - 10] + b$, with a and b taken at the corresponding galaxy population and redshifts from Table 2 in Suess et al. (2019a). The resulting r are of the order of $\approx 0.7 - 0.8$. Since there are no available relations for r at $z \gtrsim 3$, we applied the relation valid in the redshift range 2.0 - 2.5 for the two samples at $z \sim 3.3$ and 4 from Esdaile et al. (2020) and Kubo et al. (2018), resulting in values of r of 0.8 - 0.9.

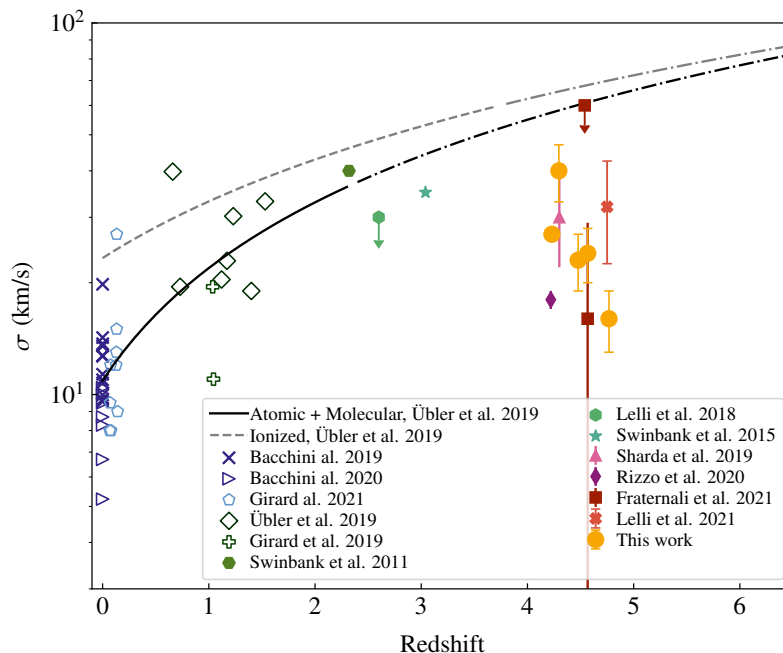


Figure 9. Location on the velocity dispersion versus redshift plane of the source galaxies in our extended sample. The values of σ_{ext} (column 6 in Table 8 and column 4 in Table 7) are shown here. The blue crosses are velocity dispersions from HI data (Bacchini et al. 2019). The empty markers are CO velocity dispersions for main-sequence galaxies (Bacchini et al. 2020; Girard et al. 2019, 2018; Übler et al. 2018; Girard et al. 2018). The filled markers are velocity dispersions for DSFGs from CO transitions (Swinbank et al. 2011, 2015; Sharda et al. 2019), [CI] (Lelli et al. 2018) or [CII] emission lines (Fraternali et al. 2021; Rizzo et al. 2020; Lelli et al. 2021). The black solid and gray dotted lines show the best-fit relations to velocity dispersions measured from warm ionized tracers ($\text{H}\alpha$, [OII], [OIII]) and atomic (HI)/molecular (CO) tracers (Übler et al. 2019). The dot-dashed lines show the corresponding extrapolations up to $z \approx 6$.

galaxies in our sample will evolve if all of their observed gas were to be converted into stars while preserving the disc configuration. This scenario is not an impossible one: while some of the gas may be expelled by galactic outflows (Nelson et al. 2019a), more could also be accreted (e.g., Bouché et al. 2010; Dekel et al. 2009). On the other hand, the sizes calculated under this assumption should be considered only as upper limits: dissipative processes lead to an accumulation of gas mainly in the central regions of galaxies, effectively shrinking the sizes of their bulges (Dekel & Burkert 2014; Zolotov et al. 2015; Tacchella et al. 2016). However, it is expected that at $z \lesssim 2$, there is a strong increase of the galaxy sizes of the quiescent population, mainly driven by dry minor mergers (e.g., Bezanson et al. 2009; Naab et al. 2009; Oser et al. 2010; Cassata et al. 2013). Panel b of Fig. 10 shows that all galaxies in our sample will end up with a stellar mass typical of the local ETGs or cSFG already at $z \approx 4$. This finding allows us to put some constraints on the physical processes (e.g., mergers, accretion, Naab et al. 2014; Bouché et al. 2010) that will be acting on these galaxies in the following ~ 12 Gyr: they should either preserve the stellar mass or be responsible only for a mild growth in size.

We note that the depletion times for our sample range from ≈ 10 to 360 Myr (see column six of Table 5), with a median value of 20 Myr. All galaxies in the sample are at $z > 4$, meaning that potentially they could be the progenitors of the recently discovered quiescent systems at $3 \lesssim z \lesssim 4$ (e.g., Glazebrook et al. 2017; Tanaka et al. 2019; Valentino et al. 2020). Unfortunately, due to the lack of instruments able to spatially resolve the restframe optical/near-infrared emission at $z \gtrsim 3$, a comparison with our DSFGs on the size-stellar mass plane is currently not feasible. However, we note that in Fig. 10, we show three samples of ten, four and five quiescent galaxies at median $z \sim 2.7$ (Lustig et al. 2020), $z \sim 3.3$

(Esdaile et al. 2020) and $z \sim 4$ (Kubo et al. 2018), respectively. For these two samples, the R_e values were derived from the rest-frame continuum emissions at ≈ 4000 , 3500 and 4200 Å, that is, the size measurements are biased towards the young stellar populations. Considering these caveats, a quantitative comparison between the high- z quiescent population and our sample of DSFGs on the size-stellar mass plane is challenging. The next generation of instruments, such as the James Webb Space Telescope (JWST, Gardner et al. 2009), will allow one to measure the structural (e.g., sizes) and the stellar-population properties of these high- z populations, facilitating further investigations of the evolutionary connection between the DSFGs and the $z \sim 3$ quiescent galaxies.

6 CONCLUSIONS

In this paper, we presented ALMA observations of the [CII] emission line for five gravitationally lensed dusty star-forming galaxies at redshift between 4 and 5. Using our lens and kinematic modelling technique, we reconstructed the background sources and inferred their kinematic and dynamical properties on ~ 200 -pc scales. By combining these observations and analysis with those from Rizzo et al. (2020) for the lensed galaxy SPT0418-47, we have thus built a sample of six DSFGs. This is the largest sample of $z \sim 4$ galaxies with such high-quality data and spatial resolutions of their [CII] line emission to date. In addition, when feasible, we also include in our sample four non-lensed DSFGs for which accurate kinematic measurements were derived (Sharda et al. 2019; Fraternali et al. 2021; Lelli et al. 2021).

The measurement of the rotation velocities and velocity dispersion profiles allowed us to gain insights on how the extreme

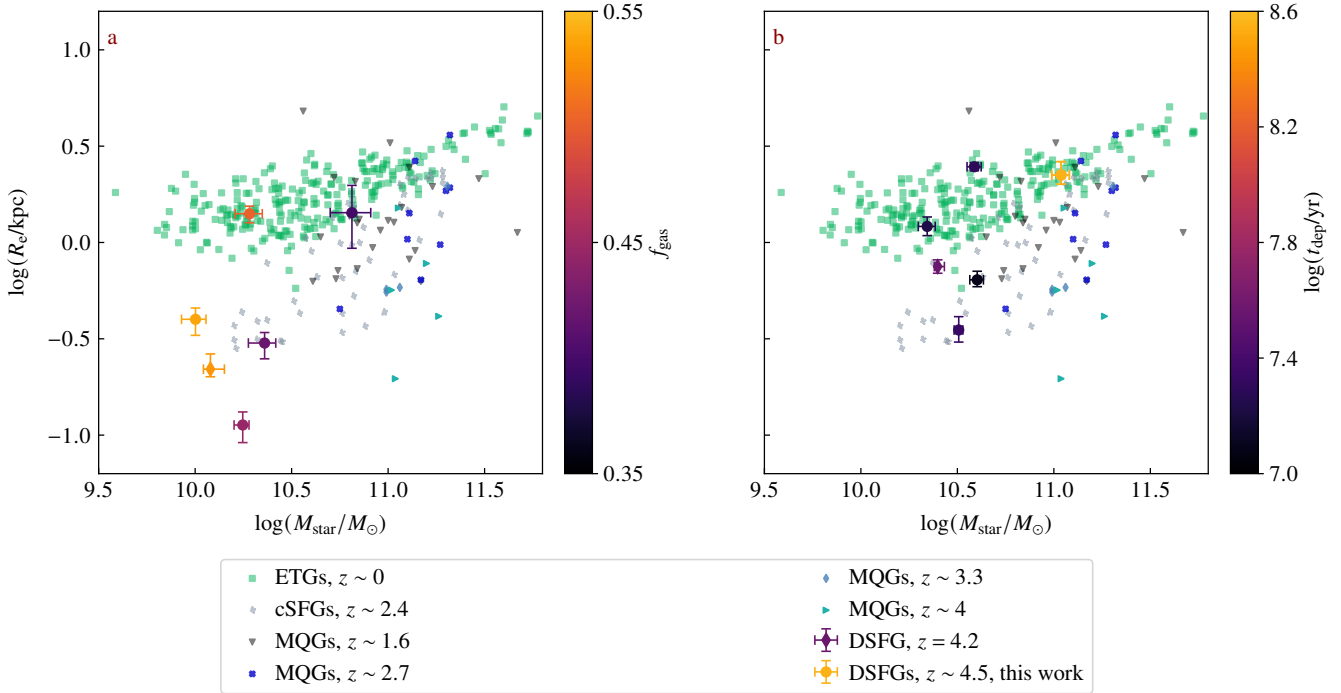


Figure 10. Location on the size versus stellar mass plane for the source galaxies in our sample colour-coded according to their gas fraction (panel a, see column three of Table 5) and depletion time (panel b, see column six of Table 5). In panel b, the stellar masses and sizes are obtained under the assumption that all the observed gas will be converted into stars, preserving the disc configuration (see the baryonic quantities in columns four and five of Table 5). Under this assumption, the sizes should be considered as upper limits. The green squares correspond to local ETGs from the ATLAS^{3D} survey (Cappellari et al. 2013), the gray stars are the cSFGs at $z \sim 2.4$ (Barro et al. 2014) and the black triangles, cyan crosses, blue diamonds are massive quiescent galaxies at the median redshifts indicated in the legend and they are taken from Belli et al. (2017); Lustig et al. (2020); Esdaile et al. (2020); Kubo et al. (2018), respectively.

astrophysical processes and conditions characterising the early Universe affect the properties of these young galaxies. In particular, the sample studied in this paper allowed us to confirm a previous finding (Rizzo et al. 2020): DSFGs have V/σ in the range 7 to 15 and median velocity dispersion in the range between ≈ 30 and ≈ 60 km s^{-1} . To date, such dynamically cold galaxies with the measured values of SFR and gas fractions are not predicted by any model (e.g., Pillepich et al. 2019; Hung et al. 2019; Dekel et al. 2020). By investigating the velocity dispersions and SFR of the studied galaxies, we found that stellar feedback mechanisms are able to sustain the level of observed turbulence with low efficiency. There is, therefore, no need of additional drivers of turbulence, such as gravitational instabilities. We then compare the velocity dispersions in our sample with the analogue measurements from the literature for galaxies at lower redshifts and with the empirical $\sigma - z$ relation found by Übler et al. (2019) for normal main-sequence galaxies up to $z \lesssim 3$. The median values of the velocity dispersions in our sample is only a factor of ≈ 2 larger than the typical HI velocity dispersions of local spiral galaxies and consistent with the CO velocity dispersions found in star-forming galaxies at $1 \lesssim z \lesssim 2$. We find that the extrapolation of the Übler et al. (2019) $\sigma - z$ relation to the redshifts studied in this paper results in a systematic overestimation of the observed velocity dispersions by a median factor of ≈ 2 .

The rotation curves of the galaxies analysed here have shapes similar to those of local spirals: they flatten at large radii and show a variety of behaviours in the inner regions, from slow to steeply rising. This similarity implies that the dynamical structures of local galaxies were already in place at higher redshifts. On the other hand,

the individuality of the observed rotation curves can be explained by the difference in the dynamical parameters defining the stellar, gas, and dark matter halo distributions.

The lack of spatially-resolved optical/near-infrared data prevented us from making sophisticated assumptions on the stellar distribution. We thus decomposed the rotation curve of our galaxies using a single Sérsic profile for the stellar component, an NFW for the dark matter halo, and an exponential disc for the gas, as traced by the [CII] line emission. From the dynamical fitting, we found that the galaxies in our sample have a stellar-mass between $\sim 1 \times 10^{10} M_{\odot}$ and $\sim 7 \times 10^{10} M_{\odot}$. Their gas fraction ranges between 0.4 and 0.6. Furthermore, four out of six galaxies have a stellar component which is well described by a Sérsic index of $n \gtrsim 2$.

This analysis allowed us to put constraints on the mechanisms responsible for the transformation of these galaxies into their most plausible descendants, the quiescent systems observed at $z \lesssim 3$. In particular, by comparing our sample with local ETGs and $z \sim 2$ cSFGs in the size-stellar mass plane, we found that two galaxies in our sample, SPT0113-46 and SPT2132-58, have sizes and stellar masses consistent with the low- z samples, two galaxies are consistent with the low-mass end of the cSFGs, while the others cover the low-mass, small-size region. Interestingly, SPT0113-46 has the lowest gas fraction within our sample and, is the only galaxy on the main sequence. All these properties seem to be indicating that SPT0113-46 is in the process of consuming its residual gas, quenching its star formation and transforming into a typical ETG. We also found that the baryonic masses in our sample are all consistent with those of local ETGs. This result allowed us to set constraints on

the small amount of baryonic matter that can be accreted in the following ~ 12 Gyr of the lifetime of these galaxies.

Our results are based on just ten galaxies. While statistically significant conclusions can not be drawn, these first results are promising. In the near future, the thousands of strong gravitationally lensed galaxies (Oguri & Marshall 2010; Collett 2015; McKean et al. 2015) discovered by the Euclid space telescope⁸, the Rubin Observatory⁹ and the Square Kilometer Array¹⁰, combined with the capability of ALMA and JWST will provide us with the opportunity to fully characterise the structural and dynamical properties on large sample of galaxies up to the epoch of reionization.

ACKNOWLEDGEMENTS

We thank the anonymous referee for a careful reading and helpful feedback. FR is grateful to Cecilia Bacchini and Francesco Valentino for useful comments and discussions and to Federico Lelli for providing the kinematic data on ALESS073.1. We also acknowledge the support of Mahsa Kohandel, Andrea Ferrara, Andrea Pallottini and Livia Vallini.

This project has received funding from the European Union's Horizon 2020 research and innovation program under the Marie Skłodowska-Curie grant agreement No. 847523 'INTERACTIONS'. SV thanks the Max Planck Society for support through a Max Planck Lise Meitner Group, and acknowledges funding from the European Research Council (ERC) under the European Union's Horizon 2020 research and innovation programme (LEDA: grant agreement No 758853). FF acknowledges support from the Friedrich Wilhelm Bessel Research Award Programme of the Alexander von Humboldt.

This research made use of Astropy and Matplotlib packages for Python (Astropy Collaboration et al. 2018).

DATA AVAILABILITY

The data underlying this article are available in the ALMA Science Archive, at <https://almascience.eso.org/asax/>. This work makes use of the following ALMA data: ADS/JAO.ALMA#2016.1.01499.S. ALMA is a partnership of ESO (representing its member states), NSF (USA) and NINS (Japan), together with NRC (Canada), NSC and ASIAA (Taiwan), and KASI (Republic of Korea), in cooperation with the Republic of Chile. The Joint ALMA Observatory is operated by ESO, AUI/NRAO and NAOJ.

REFERENCES

Aravena M., et al., 2016, *Mon. Not. R. Astron. Soc.*, **457**, 4406
 Arribas S., Colina L., Bellocchi E., Maiolino R., Villar-Martín M., 2014, *A&A*, **568**, A14
 Astropy Collaboration et al., 2018, *AJ*, **156**, 123
 Bacchini C., Fraternali F., Iorio G., Pezzulli G., 2019, *A&A*, **622**, A64
 Bacchini C., Fraternali F., Iorio G., Pezzulli G., Marasco A., Nipoti C., 2020, arXiv e-prints, p. [arXiv:2006.10764](https://arxiv.org/abs/2006.10764)
 Barro G., et al., 2014, *Astrophys. J.*, **791**, 52
 Behroozi P., Wechsler R. H., Hearin A. P., Conroy C., 2019, *MNRAS*, **488**, 3143

⁸ <https://www.euclid-ec.org>

⁹ <https://www.lsst.org>

¹⁰ <https://www.skatelescope.org>

Belli S., Newman A. B., Ellis R. S., 2017, *ApJ*, **834**, 18
 Bezanson R., van Dokkum P. G., Tal T., Marchesini D., Kriek M., Franx M., Coppi P., 2009, *ApJ*, **697**, 1290
 Binney J., Tremaine S., 2008, *Galactic Dynamics: Second Edition*
 Bisigello L., Caputi K. I., Grogan N., Koekemoer A., 2018, *A&A*, **609**, A82
 Bothwell M. S., et al., 2017, *MNRAS*, **466**, 2825
 Bouché N., et al., 2010, *ApJ*, **718**, 1001
 Bouché N., Carfantan H., Schroetter I., Michel-Dansac L., Contini T., 2015, *AJ*, **150**, 92
 Bournaud F., Elmegreen B. G., Martig M., 2009, *ApJ*, **707**, L1
 Brinchmann J., Charlot S., White S. D. M., Tremonti C., Kauffmann G., Heckman T., Brinkmann J., 2004, *MNRAS*, **351**, 1151
 Brooks A., Christensen C., 2016, *Bulge Formation via Mergers in Cosmological Simulations*. p. 317, doi:10.1007/978-3-319-19378-6_12
 Cappellari M., et al., 2013, *Mon. Not. R. Astron. Soc.*, **432**, 1709
 Caputi K. I., et al., 2017, *ApJ*, **849**, 45
 Carlstrom J. E., et al., 2011, *Publ. Astron. Soc. Pac.*, **123**, 568
 Carniani S., et al., 2013, *A&A*, **559**, A29
 Cassata P., et al., 2013, *ApJ*, **775**, 106
 Chisholm J., Tremonti C. A., Leitherer C., Chen Y., 2017, *MNRAS*, **469**, 4831
 Cicone C., Maiolino R., Marconi A., 2016, *A&A*, **588**, A41
 Cimatti A., Fraternali F., Nipoti C., 2019, *Introduction to Galaxy Formation and Evolution: From Primordial Gas to Present-Day Galaxies*
 Circosta C., et al., 2019, *A&A*, **623**, A172
 Collett T. E., 2015, *ApJ*, **811**, 20
 Concas A., Popesso P., Brusa M., Mainieri V., Erfanianfar G., Morselli L., 2017, *A&A*, **606**, A36
 Cormier D., et al., 2015, *A&A*, **578**, A53
 Crain R. A., et al., 2015, *MNRAS*, **450**, 1937
 De Breuck C., Maiolino R., Caselli P., Coppin K., Hailey-Dunsheath S., Nagao T., 2011, *A&A*, **530**, L8
 De Breuck C., et al., 2014, *A&A*, **565**, A59
 De Breuck C., et al., 2019, *A&A*, **631**, A167
 Dekel A., Burkert A., 2014, *Mon. Not. R. Astron. Soc.*, **438**, 1870
 Dekel A., et al., 2009, *Nature*, **457**, 451
 Dekel A., Ginzburg O., Jiang F., Freundlich J., Lapiner S., Ceverino D., Primack J., 2020, *MNRAS*, **493**, 4126
 Di Teodoro E. M., Fraternali F., 2015, *MNRAS*, **451**, 3021
 Di Teodoro E. M., Fraternali F., Miller S. H., 2016, *Astron. Astrophys.*, **594**, A77
 Di Teodoro E. M., et al., 2018, *MNRAS*, **476**, 804
 Dimauro P., et al., 2019, *MNRAS*, **489**, 4135
 Dutton A. A., Macciò A. V., 2014, *Mon. Not. R. Astron. Soc.*, **441**, 3359
 Eliche-Moral M. C., Rodríguez-Pérez C., Borlaff A., Querejeta M., Tapia T., 2018, *A&A*, **617**, A113
 Elmegreen B. G., Bournaud F., Elmegreen D. M., 2008, *ApJ*, **688**, 67
 Erwin P., Debattista V. P., 2017, *MNRAS*, **468**, 2058
 Esdaile J., et al., 2020, arXiv e-prints, p. [arXiv:2010.09738](https://arxiv.org/abs/2010.09738)
 Faucher-Giguère C.-A., Quataert E., Hopkins P. F., 2013, *MNRAS*, **433**, 1970
 Fraternali F., Binney J. J., 2006, *MNRAS*, **366**, 449
 Fraternali F., Oosterloo T., Sancisi R., van Moorsel G., 2001, *ApJ*, **562**, L47
 Fraternali F., van Moorsel G., Sancisi R., Oosterloo T., 2002, *AJ*, **123**, 3124
 Fraternali F., Karim A., Magnelli B., Gómez-Guijarro C., Jiménez-Andrade E. F., Poses A. C., 2021, *A&A*, **647**, A194
 Gardner J. P., et al., 2009, *Astrophysics and Space Science Proceedings*, **10**, 1
 Genzel R., et al., 2020, *ApJ*, **902**, 98
 Ginolfi M., et al., 2020, *A&A*, **633**, A90
 Girard M., et al., 2018, *A&A*, **613**, A72
 Girard M., et al., 2021, arXiv e-prints, p. [arXiv:2101.04122](https://arxiv.org/abs/2101.04122)
 Glazebrook K., et al., 2017, *Nature*, **544**, 71
 Glover S. C. O., Smith R. J., 2016, *MNRAS*, **462**, 3011
 Gómez-Guijarro C., et al., 2018, *ApJ*, **856**, 121
 Gullberg B., et al., 2018, *Astrophys. J.*, **859**, 12
 Harrison C. M., et al., 2017, *Mon. Not. R. Astron. Soc.*, **467**, 1965
 Hatziminaoglou E., et al., 2015, *The Messenger*, **162**, 24

- Hayward C. C., Hopkins P. F., 2017, *Mon. Not. R. Astron. Soc.*, **465**, 1682
- Hodge J. A., da Cunha E., 2020, arXiv e-prints, p. arXiv:2004.00934
- Hodge J. A., Carilli C. L., Walter F., de Blok W. J. G., Riechers D., Daddi E., Lentati L., 2012, *ApJ*, **760**, 11
- Hodge J. A., Riechers D., Decarli R., Walter F., Carilli C. L., Daddi E., Dannerbauer H., 2015, *Astrophys. J. Lett.*, **798**, L18
- Hodge J. A., et al., 2016, *ApJ*, **833**, 103
- Hodge J. A., et al., 2019, *ApJ*, **876**, 130
- Högbom J. A., 1974, *Astron. Astrophys. Sup.*, **15**, 417
- Hopkins P. F., Quataert E., Murray N., 2012, *MNRAS*, **421**, 3522
- Hopkins P. F., Cox T. J., Hernquist L., Narayanan D., Hayward C. C., Murray N., 2013, *MNRAS*, **430**, 1901
- Hung C.-L., et al., 2019, *Mon. Not. R. Astron. Soc.*, **482**, 5125
- Iorio G., Fraternali F., Nipoti C., Di Teodoro E., Read J. I., Battaglia G., 2017, *Mon. Not. R. Astron. Soc.*, **466**, 4159
- Johnson H. L., et al., 2018, *MNRAS*, **474**, 5076
- Jones G. C., et al., 2017, *ApJ*, **850**, 180
- Kennicutt R. C., Evans N. J., 2012, *Annu. Rev. Astron. Astr.*, **50**, 531
- Kim C.-G., Ostriker E. C., 2018, *ApJ*, **853**, 173
- Kohandel M., Pallottini A., Ferrara A., Carniani S., Gallerani S., Vallini L., Zanella A., Behrens C., 2020, *MNRAS*, **499**, 1250
- Kormendy J., 2016, *Elliptical Galaxies and Bulges of Disc Galaxies: Summary of Progress and Outstanding Issues*. p. 431, doi:10.1007/978-3-319-19378-6_16
- Krajnović D., et al., 2013, *Mon. Not. R. Astron. Soc.*, **432**, 1768
- Krumholz M. R., Burkhardt B., Forbes J. C., Crocker R. M., 2018, *Mon. Not. R. Astron. Soc.*, **477**, 2716
- Kubo M., Tanaka M., Yabe K., Toft S., Stockmann M., Gómez-Guijarro C., 2018, *ApJ*, **867**, 1
- Lacey C. G., et al., 2016, *MNRAS*, **462**, 3854
- Lagos C. d. P., da Cunha E., Robotham A. S. G., Obreschkow D., Valentino F., Fujimoto S., Magdis G. E., Tobar R., 2020, *MNRAS*, **499**, 1948
- Lang P., et al., 2014, *Astrophys. J.*, **788**, 11
- Lelli F., McGaugh S. S., Schombert J. M., 2016, *AJ*, **152**, 157
- Lelli F., De Breuck C., Falkendal T., Fraternali F., Man A. W. S., Nesvadba N. P. H., Lehnert M. D., 2018, *Mon. Not. R. Astron. Soc.*, **479**, 5440
- Lelli F., Di Teodoro E. M., Fraternali F., Man A. W. S., Zhang Z.-Y., De Breuck C., Davis T. A., Maiolino R., 2021, *Science*, **371**, 713
- Levy R. C., et al., 2018, *ApJ*, **860**, 92
- Lima Neto G. B., Gerbal D., Márquez I., 1999, *Mon. Not. R. Astron. Soc.*, **309**, 481
- Litke K. C., et al., 2019, *ApJ*, **870**, 80
- Lovell M. R., et al., 2018, *MNRAS*, **481**, 1950
- Lustig P., et al., 2020, *MNRAS*.
- Ma J., et al., 2015, *ApJ*, **812**, 88
- Madden S. C., et al., 2020, *A&A*, **643**, A141
- Mancera Piña P. E., et al., 2019, *ApJ*, **883**, L33
- Martizzi D., Fielding D., Faucher-Giguère C.-A., Quataert E., 2016, *MNRAS*, **459**, 2311
- McAlpine S., et al., 2019, *Mon. Not. R. Astron. Soc.*, p. 1653
- McDermid R. M., et al., 2015, *Mon. Not. R. Astron. Soc.*, **448**, 3484
- McKean J., et al., 2015, in *Advancing Astrophysics with the Square Kilometre Array (AASKA14)*. p. 84 (arXiv:1502.03362)
- McMullin J. P., Waters B., Schiebel D., Young W., Golap K., 2007, in *Shaw R. A., Hill F., Bell D. J., eds, Astronomical Society of the Pacific Conference Series Vol. 376, Astr. Soc. P.* p. 127
- McQuinn K. B. W., van Zee L., Skillman E. D., 2019, *ApJ*, **886**, 74
- Mogotsi K. M., de Blok W. J. G., Caldu-Primo A., Walter F., Ianjamasimanana R., Leroy A. K., 2016, *AJ*, **151**, 15
- Mosleh M., Tacchella S., Renzini A., Carollo C. M., Molaeinezhad A., Onodera M., Khosroshahi H. G., Lilly S., 2017, *ApJ*, **837**, 2
- Naab T., Ostriker J. P., 2017, *ARA&A*, **55**, 59
- Naab T., Johansson P. H., Ostriker J. P., 2009, *Astrophys. J. Lett.*, **699**, L178
- Naab T., et al., 2014, *MNRAS*, **444**, 3357
- Narayanan D., et al., 2015, *Nature*, **525**, 496
- Navarro J. F., Frenk C. S., White S. D. M., 1996, *Astrophys. J.*, **462**, 563
- Neeleman M., Prochaska J. X., Kanekar N., Rafelski M., 2020, *Nature*, **581**, 269
- Nelson D., et al., 2019a, *MNRAS*, **490**, 3234
- Nelson E. J., et al., 2019b, *ApJ*, **870**, 130
- Noeske K. G., et al., 2007, *ApJ*, **660**, L43
- Nordon R., Sternberg A., 2016, *MNRAS*, **462**, 2804
- Oesch P. A., et al., 2010, *ApJ*, **714**, L47
- Oguri M., Marshall P. J., 2010, *MNRAS*, **405**, 2579
- Ohlin L., Renaud F., Agertz O., 2019, *MNRAS*, **485**, 3887
- Oser L., Ostriker J. P., Naab T., Johansson P. H., Burkert A., 2010, *ApJ*, **725**, 2312
- Ostriker E. C., Shetty R., 2011, *ApJ*, **731**, 41
- Pallottini A., et al., 2019, *MNRAS*, **487**, 1689
- Papadopoulos P. P., Thi W. F., Viti S., 2002, *ApJ*, **579**, 270
- Pillepich A., et al., 2019, arXiv e-prints, p. arXiv:1902.05553
- Pineda J. L., Langer W. D., Velusamy T., Goldsmith P. F., 2013, *A&A*, **554**, A103
- Planck Collaboration et al., 2016, *A&A*, **594**, A13
- Posti L., Fraternali F., Marasco A., 2019, *A&A*, **626**, A56
- Powell D., Vegetti S., McKean J. P., Spingola C., 2020, arXiv e-prints, p. arXiv:2005.03609
- Renzini A., et al., 2015, *MNRAS*, **454**, 4197
- Reuter C., et al., 2020, *ApJ*, **902**, 78
- Rigopoulou D., et al., 2014, *ApJ*, **781**, L15
- Rix H.-W., Guhathakurta P., Colless M., Ing K., 1997, *MNRAS*, **285**, 779
- Rizzo F., Vegetti S., Fraternali F., Di Teodoro E., 2018, *Mon. Not. R. Astron. Soc.*, **481**, 5606
- Rizzo F., Vegetti S., Powell D., Fraternali F., McKean J. P., Stacey H. R., White S. D. M., 2020, *Nature*, **584**, 201
- Robertson B., Bullock J. S., Cox T. J., Di Matteo T., Hernquist L., Springel V., Yoshida N., 2006, *ApJ*, **645**, 986
- Rodriguez-Gomez V., et al., 2016, *MNRAS*, **458**, 2371
- Romeo A. B., Falstad N., 2013, *MNRAS*, **433**, 1389
- Sancisi R., Fraternali F., Oosterloo T., van der Hulst T., 2008, *A&ARv*, **15**, 189
- Sargsyan L., Samsyan A., Leboutteiller V., Weedman D., Barry D., Bernard-Salas J., Houck J., Spoon H., 2014, *ApJ*, **790**, 15
- Satyapal S., Ellison S. L., McAlpine W., Hickox R. C., Patton D. R., Mendel J. T., 2014, *MNRAS*, **441**, 1297
- Schneider P., 2006, in *Meylan G., Jetzer P., North P., Schneider P., Kochanek C. S., Wambsgans J., eds, Saas-Fee Advanced Course 33: Gravitational Lensing: Strong, Weak and Micro*. pp 1–89
- Sharda P., et al., 2019, *MNRAS*, **487**, 4305
- Silk J., 2013, *ApJ*, **772**, 112
- Smit R., et al., 2018, *Nature*, **553**, 178
- Sommovigo L., Ferrara A., Carniani S., Zanella A., Pallottini A., Gallerani S., Vallini L., 2021, *MNRAS*, **503**, 4878
- Speagle J. S., 2019, arXiv e-prints, p. arXiv:1904.02180
- Spilker J. S., et al., 2016, *Astrophys. J.*, **826**, 112
- Spilker J. S., et al., 2020, *ApJ*, **905**, 86
- Stacey G. J., Hailey-Dunsheath S., Ferkinhoff C., Nikola T., Parshley S. C., Benford D. J., Staguhn J. G., Fiolet N., 2010a, *ApJ*, **724**, 957
- Stacey G. J., Hailey-Dunsheath S., Ferkinhoff C., Nikola T., Parshley S. C., Benford D. J., Staguhn J. G., Fiolet N., 2010b, *Astrophys. J.*, **724**, 957
- Stacey H. R., et al., 2020, arXiv e-prints, p. arXiv:2009.01277
- Stanley F., Jolly J. B., König S., Knudsen K. K., 2019, *A&A*, **631**, A78
- Steinhardt C. L., et al., 2014, *ApJ*, **791**, L25
- Strandet M. L., et al., 2016, *ApJ*, **822**, 80
- Suess K. A., Kriek M., Price S. H., Barro G., 2019a, *ApJ*, **877**, 103
- Suess K. A., Kriek M., Price S. H., Barro G., 2019b, *ApJ*, **885**, L22
- Swinbank A. M., et al., 2011, *ApJ*, **742**, 11
- Swinbank A. M., et al., 2012a, *MNRAS*, **427**, 1066
- Swinbank A. M., Smail I., Sobral D., Theuns T., Best P. N., Geach J. E., 2012b, *ApJ*, **760**, 130
- Swinbank A. M., et al., 2015, *ApJ*, **806**, L17
- Swinbank A. M., et al., 2017, *MNRAS*, **467**, 3140
- Tacchella S., Dekel A., Carollo C. M., Ceverino D., DeGraf C., Lapiner S., Mandelker N., Primack J. R., 2016, *MNRAS*, **458**, 242
- Tacchella S., et al., 2018, *ApJ*, **859**, 56
- Tadaki K., et al., 2018, *Nature*, **560**, 613

- Tadaki K.-i., et al., 2020, *ApJ*, 889, 141
- Tamburro D., Rix H. W., Leroy A. K., Mac Low M. M., Walter F., Kennicutt R. C., Brinks E., de Blok W. J. G., 2009, *AJ*, 137, 4424
- Tanaka M., et al., 2019, *ApJ*, 885, L34
- Tasca L. A. M., et al., 2015, *A&A*, 581, A54
- Teklu A. F., Remus R.-S., Dolag K., Arth A., Burkert A., Obreja A., Schulze F., 2018, *Astrophys. J. Lett.*, 854, L28
- Terzić B., Graham A. W., 2005, *Mon. Not. R. Astron. Soc.*, 362, 197
- Toft S., Gallazzi A., Zirm A., Wold M., Zibetti S., Grillo C., Man A., 2012, *ApJ*, 754, 3
- Tortora C., Napolitano N. R., Cardone V. F., Capaccioli M., Jetzer P., Molinaro R., 2010, *MNRAS*, 407, 144
- Turner O. J., et al., 2017, *Mon. Not. R. Astron. Soc.*, 471, 1280
- Übler H., et al., 2017, *ApJ*, 842, 121
- Übler H., et al., 2018, *Astrophys. J. Lett.*, 854, L24
- Übler H., et al., 2019, *Astrophys. J.*, 880, 48
- Utomo D., Blitz L., Falgarone E., 2019, *ApJ*, 871, 17
- Valentino F., et al., 2020, *ApJ*, 889, 93
- Varidel M. R., et al., 2020, *MNRAS*, 495, 2265
- Vegetti S., Koopmans L. V. E., 2009, *Mon. Not. R. Astron. Soc.*, 392, 945
- Vieira J. D., et al., 2010, *ApJ*, 719, 763
- Vieira J. D., et al., 2013, *Nature*, 495, 344
- Vogelsberger M., Marinacci F., Torrey P., Puchwein E., 2020, *Nature Reviews Physics*, 2, 42
- Weiß A., et al., 2013, *Astrophys. J.*, 767, 88
- Whitaker K. E., van Dokkum P. G., Brammer G., Franx M., 2012, *ApJ*, 754, L29
- Wisnioski E., et al., 2015, *ApJ*, 799, 209
- Wisnioski E., et al., 2019, *ApJ*, 886, 124
- Wolfire M. G., Hollenbach D., McKee C. F., 2010, *ApJ*, 716, 1191
- Wootten A., Thompson A. R., 2009, *IEEE Proceedings*, 97, 1463
- Zanella A., et al., 2018, *Mon. Not. R. Astron. Soc.*, 481, 1976
- Zolotov A., et al., 2015, *Mon. Not. R. Astron. Soc.*, 450, 2327
- van Dokkum P. G., et al., 2015, *ApJ*, 813, 23
- van der Wel A., et al., 2014, *Astrophys. J.*, 788, 28

APPENDIX A: TESTS ON THE KINEMATIC HYPERPRIOR

The methodology used to derive the kinematics of the lensed galaxies was described [Rizzo et al. \(2018\)](#), where also extensive tests on mock data containing lensed galaxies with different kinematic and geometric properties were discussed. To summarize, with this methodology, one is able to derive the rotation velocity and velocity dispersion as well as the geometry of lensed galaxies. For the latter, [Rizzo et al. \(2018\)](#) performed tests on galaxies with a variety of inclinations, from $i \sim 40$ deg to $i \sim 80$ deg (nearly edge-on), as well as on galaxies with warps in their position angles. The mock data analyzed in [Rizzo et al. \(2018\)](#) have also a variety of V/σ , from ~ 2 up to 10.

We have now extended the tests in [Rizzo et al. \(2018\)](#) to mock data containing a lensed dispersion-dominated galaxy with $V/\sigma \sim 0.3$ and to real observations of a lensed merging system. In the first case, we found the residuals are at the noise level and the input parameters are recovered with accuracies of the order of 2%, consistent with the values reported in [Rizzo et al. \(2018\)](#). We note that in the literature, there also are a number of non-lensed galaxies that are fitted using a tilted ring model and with resulting $V/\sigma \lesssim 2$ ([Iorio et al. 2017](#); [Mancera Piña et al. 2019](#)). In other words, a galaxy well described by a rotating disc is not necessarily a galaxy with high V/σ ratio. (Fig. A1) In the second case, we model the ALMA [CII] observations of SPT0346-52, a DSFG that was previously identified as a close-in merger ([Litke et al. 2019](#)). Consistently with this previous

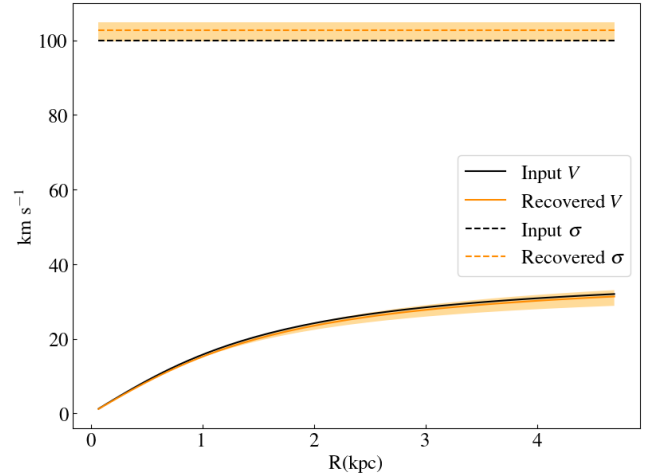


Figure A1. The black solid and dashed lines show the input profiles of the rotation velocity and velocity dispersion profiles used to create mock data of a lensed dispersion-dominated galaxy. The orange solid and dashed lines show the recovered profiles and the corresponding uncertainties.

finding ([Litke et al. 2019](#)), we found that a rotating disc is not a good description of this DSFG for the following reasons:

- the residuals are at the noise level when we model the data without the inclusion of a kinematic hyperprior on the source. Systematic residuals up to the $5\text{-}\sigma$ levels appear, instead, when the source is reconstructed using a rotating disc as regularising prior for the source reconstruction (see red spots in column three in Fig. A2);
- the p-v diagram along the minor axis show features that are not reproduced by a rotating disc (Fig. A3);
- we infer a rotation velocity of $\sim 700 \text{ km s}^{-1}$. This value is unphysical and it is a clear hint that SPT0346-52 is a merging system.

Overall, this test shows that, even if we use a rotating disc as a hyperprior for the source reconstruction, we are able to distinguish whether a rotating disc is not a good description of the lensed galaxy by comparing the source reconstruction and the residuals obtained with and without the source hyperprior. We have also performed tests on mock observations from the SERRA simulation ([Pallottini et al. 2019](#)), which confirm the above results and will be presented in a follow-up paper.

APPENDIX B: LENS AND KINEMATIC MODELS

In this section, we show the outputs of the lens and kinematic for each galaxy of the sample. As for SPT0113-46 in Section 3.2 (Fig. 1 - 3), we show three sets of figures: the moment map of the lensed galaxies, the corresponding reconstructed source and kinematic model (Figs. B1-B4); some representative channel maps from the cubes containing the data, the model, the residuals, the source and the kinematic model (Figs. B5-B8); the position-velocity diagrams along the minor and major axes (Figs. B9-B12).

B1 Spatial resolution on the source plane

In order to estimate the spatial resolutions on the source plane we calculate the dimensions of the triangular grid ([Vegetti & Koopmans](#)

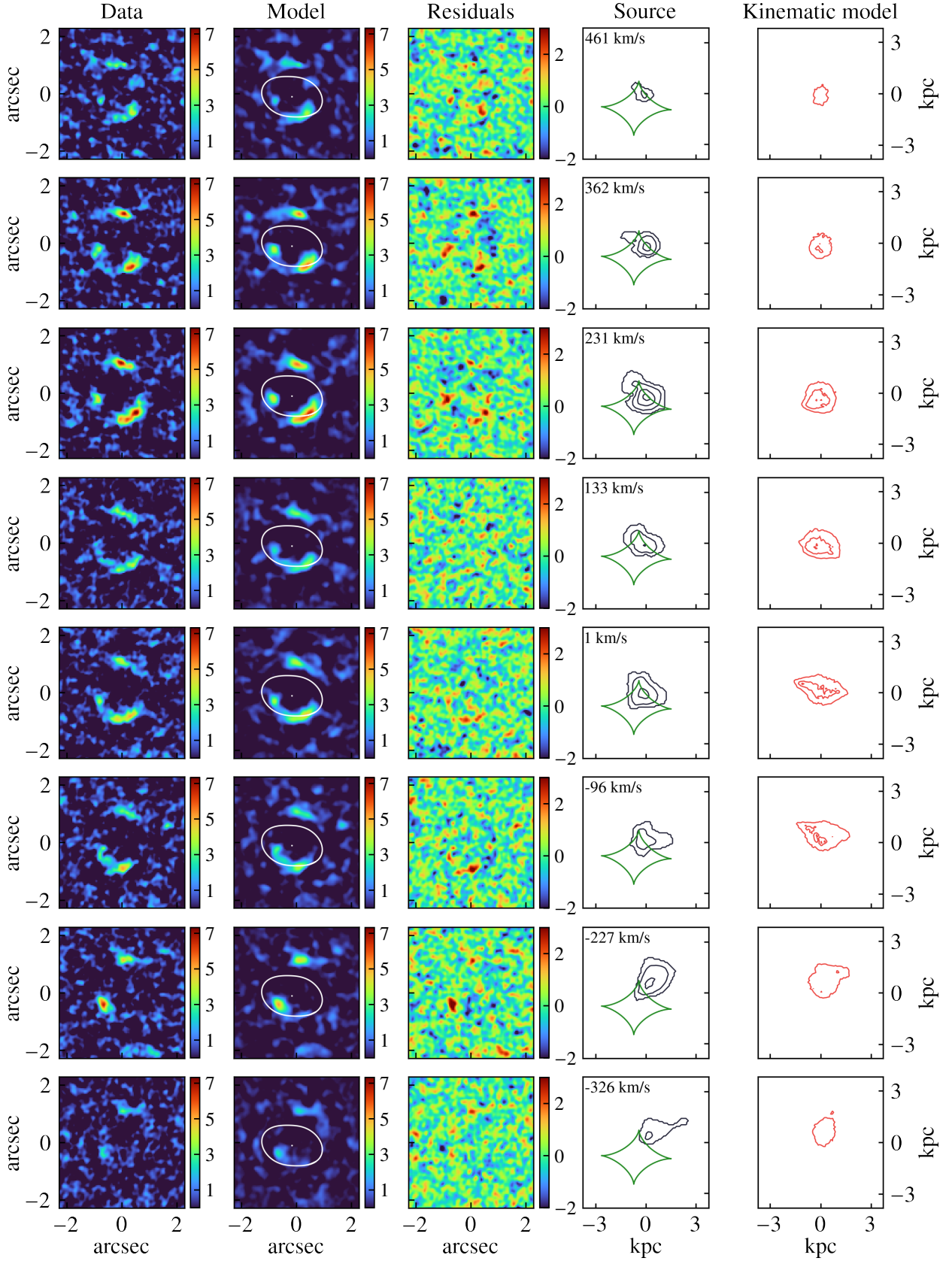


Figure A2. Channel maps for SPT0346-52. Same as in Fig. 2.

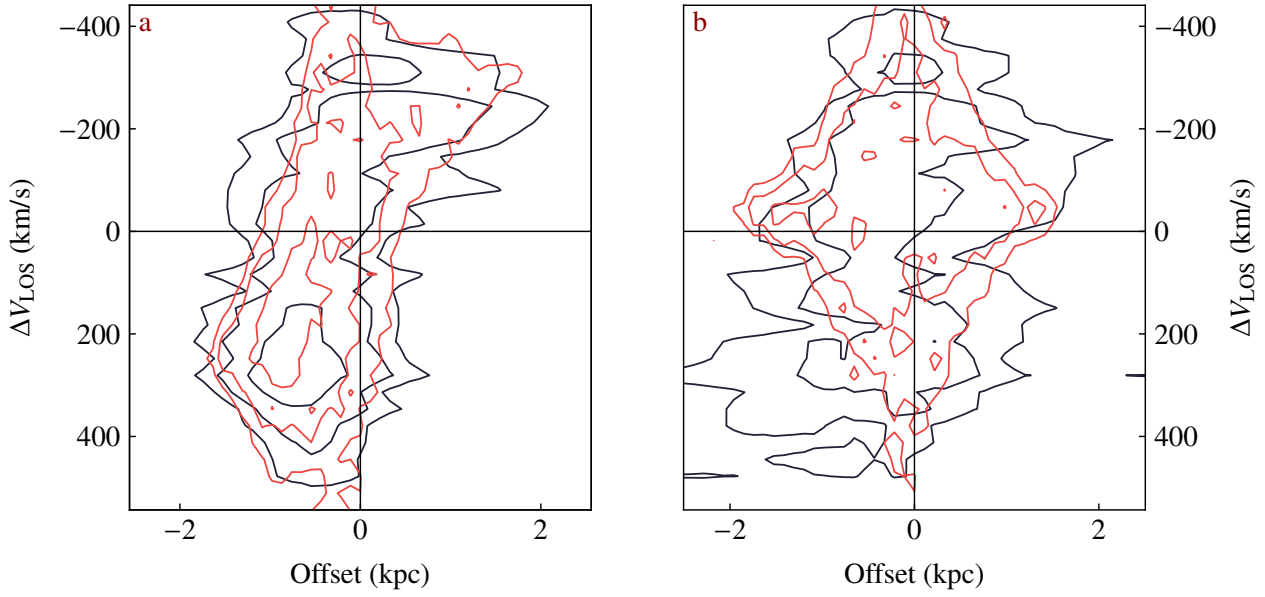


Figure A3. Position-velocity diagrams for SPT0346-52. Same as in Fig. 3.

Table B1. Statistics of the spatial resolution on the source plane.

Name	Maximum resolution pc	Median resolution pc
SPT0113-46	26	198
SPT0345-47	47	189
SPT0441-46	139	185
SPT2146-55	24	173
SPT2132-58	64	300

2009; Rizzo et al. 2018) in regions with $\text{SNR} \geq 3$ for each spectral channel of the source cube (see Section 3.2). We then verified that the recovered resolutions correspond to those obtained using the methodology described in Stacey et al. (2020). In this case, mock lensed data were created from Gaussian sources with different sizes and different locations on the source plane. The recovered source dimensions are then compared to the input Gaussian sources to infer the minimum reliable source sizes.

The minimum and median spatial resolutions for each galaxy of the sample are listed in Table B1.

APPENDIX C: PRIOR DISTRIBUTIONS FOR THE DYNAMICAL MODELLING

In Table C1, we show the values of the concentration parameters c that define the distribution of the NFW dark-matter halo, equation (10). Table C2 lists the intervals for the uniform and log-uniform (for the masses) priors employed in the dynamic fitting described in Section 3.3. Similarly to the assumption in Rizzo et al. (2020), for $\alpha_{[\text{CII}]}$ we employ a uniform prior in the range corresponding to $\pm 3\text{-}\sigma$ respect to the mean value of $30 M_{\odot}/L_{\odot}$ found by Zanella et al. (2018).

Table C1. Concentration of the NFW dark-matter haloes, fixed parameters of the dynamical models presented in Section 3.3.

Name	c
SPT0113-46	3.04
SPT0345-47	2.97
SPT0441-46	2.77
SPT2146-55	2.67
SPT2132-58	2.45

Table C2. Intervals of the prior distributions in the rotation curve decomposition (Section 3.3).

Parameter	Prior
M_{star}	$[10^7, 10^{11}] M_{\odot}$
R_{e}	$[0.04, 4.0] \text{ kpc}$
n	$[0.5, 10]$
$\alpha_{[\text{CII}]}$	$[3.8, 238.0] M_{\odot}/L_{\odot}$
M_{DM}	$[10^{10}, 10^{13}] M_{\odot}$

This paper has been typeset from a \LaTeX file prepared by the author.

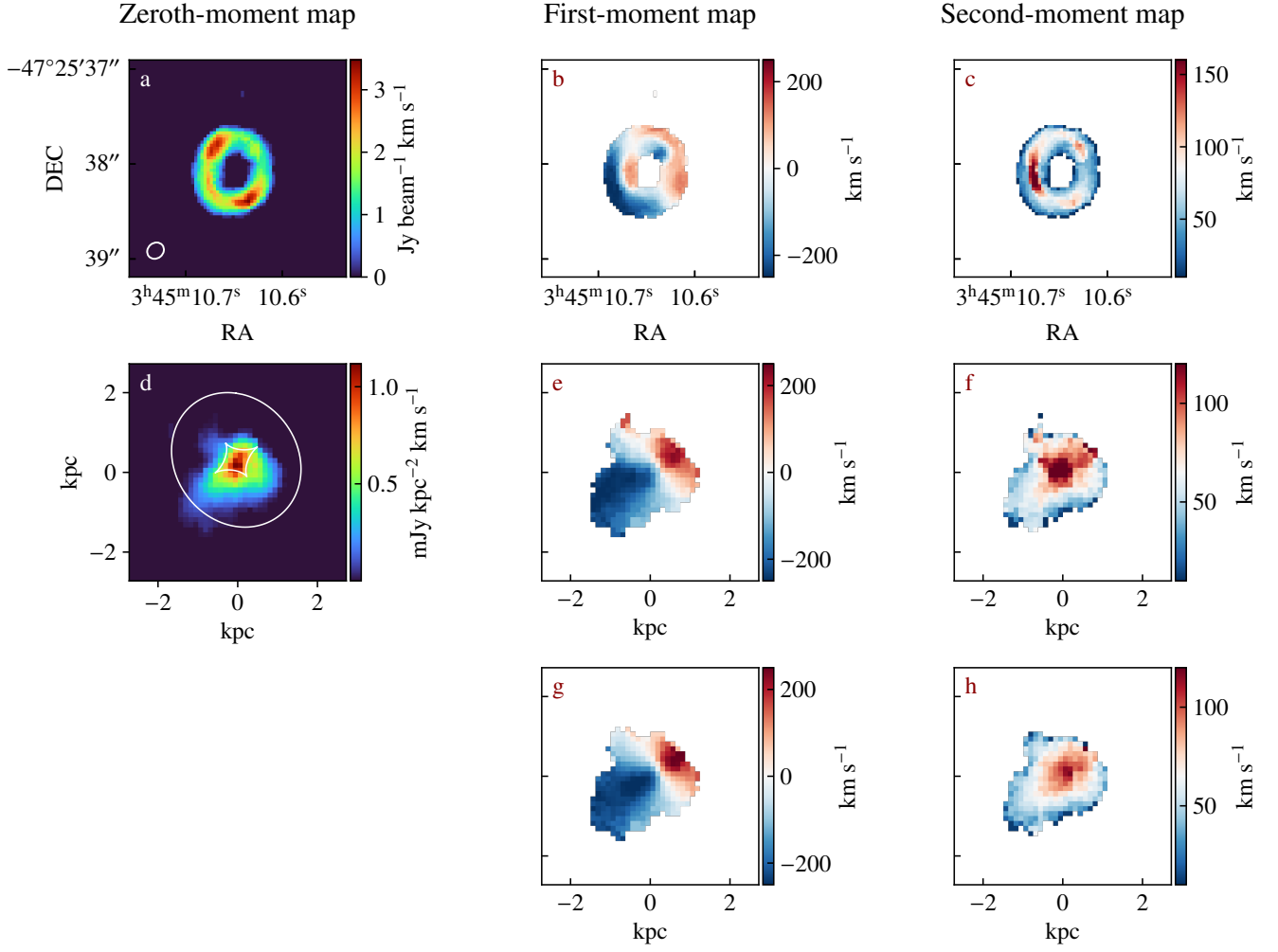


Figure B1. Moment maps for SPT0345-47. Same as in Fig. 1. The beam size, shown as a white ellipse on the lower left corner of panel a, is $0.18 \times 0.16 \text{ arcsec}^2$ at a position angle of -50.6° .

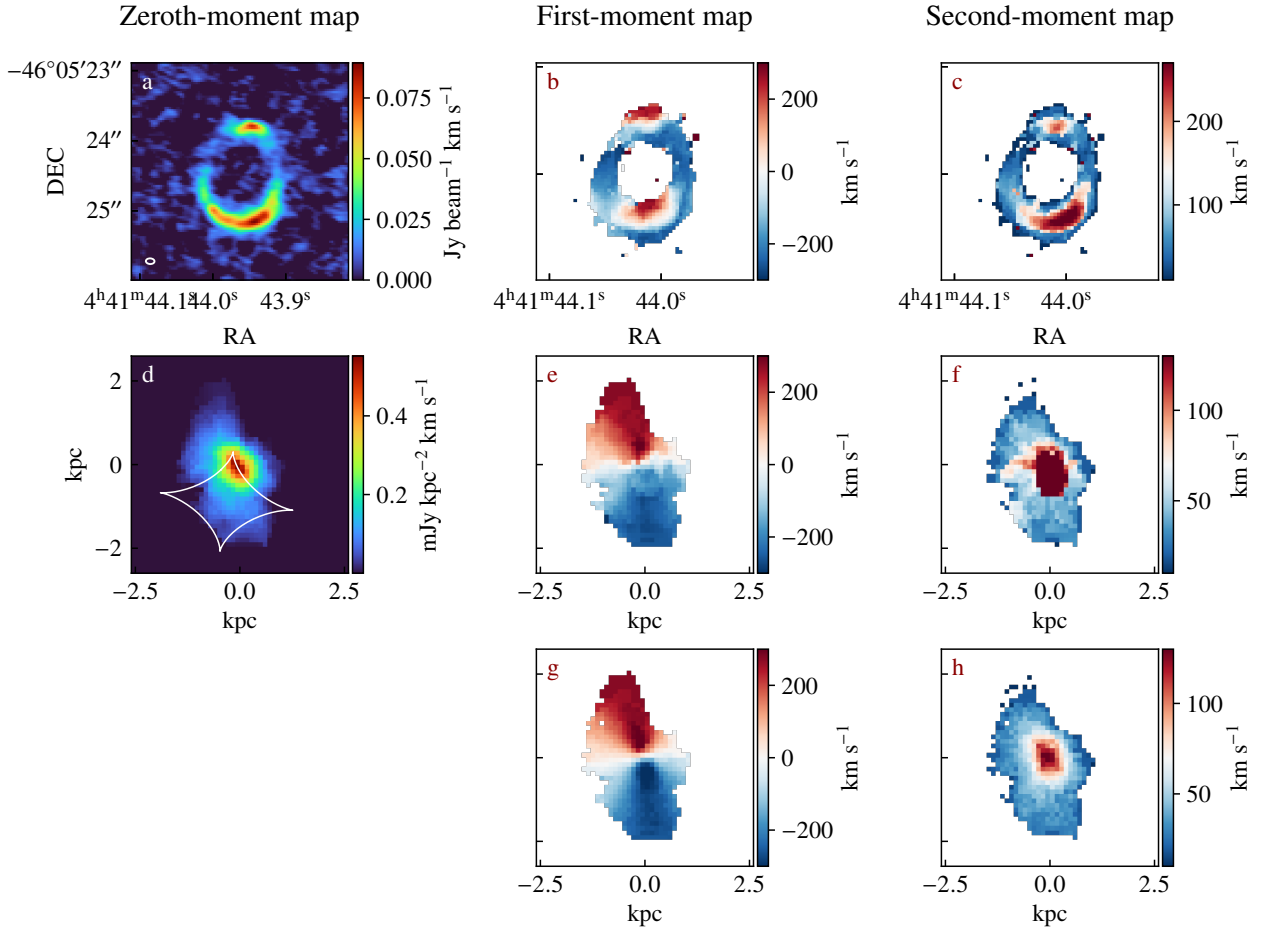


Figure B2. Moment maps for SPT0441-46. Same as in Fig. 1. The beam size, shown as a white ellipse on the lower left corner of panel a, is $0.23 \times 0.19 \text{ arcsec}^2$ at a position angle of -46.6° .

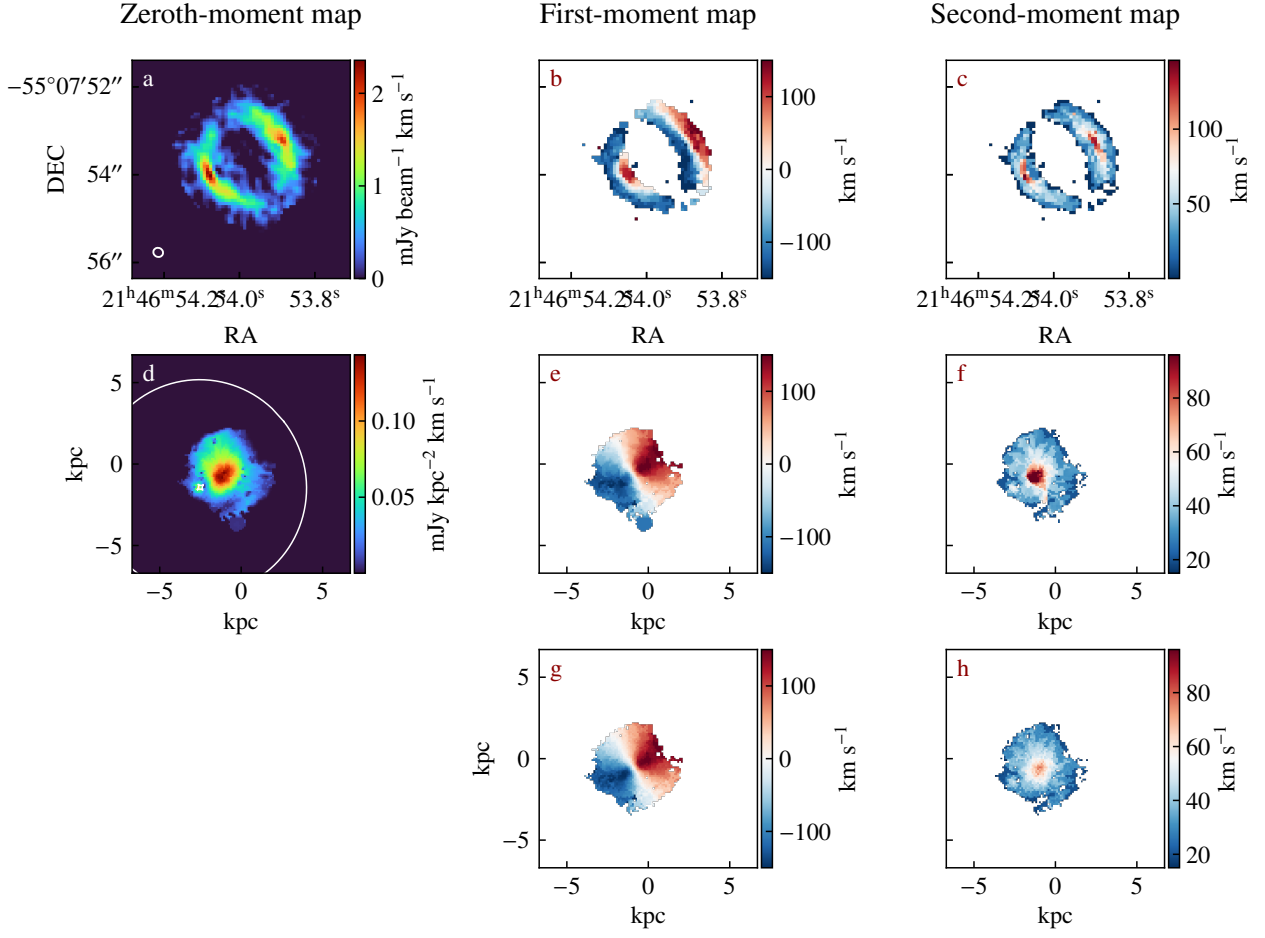


Figure B3. Moment maps for SPT2146-55. Same as in Fig. 1. The beam size, shown as a white ellipse on the lower left corner of panel a, is 0.23×0.20 arcsec² at a position angle of -64.1° .

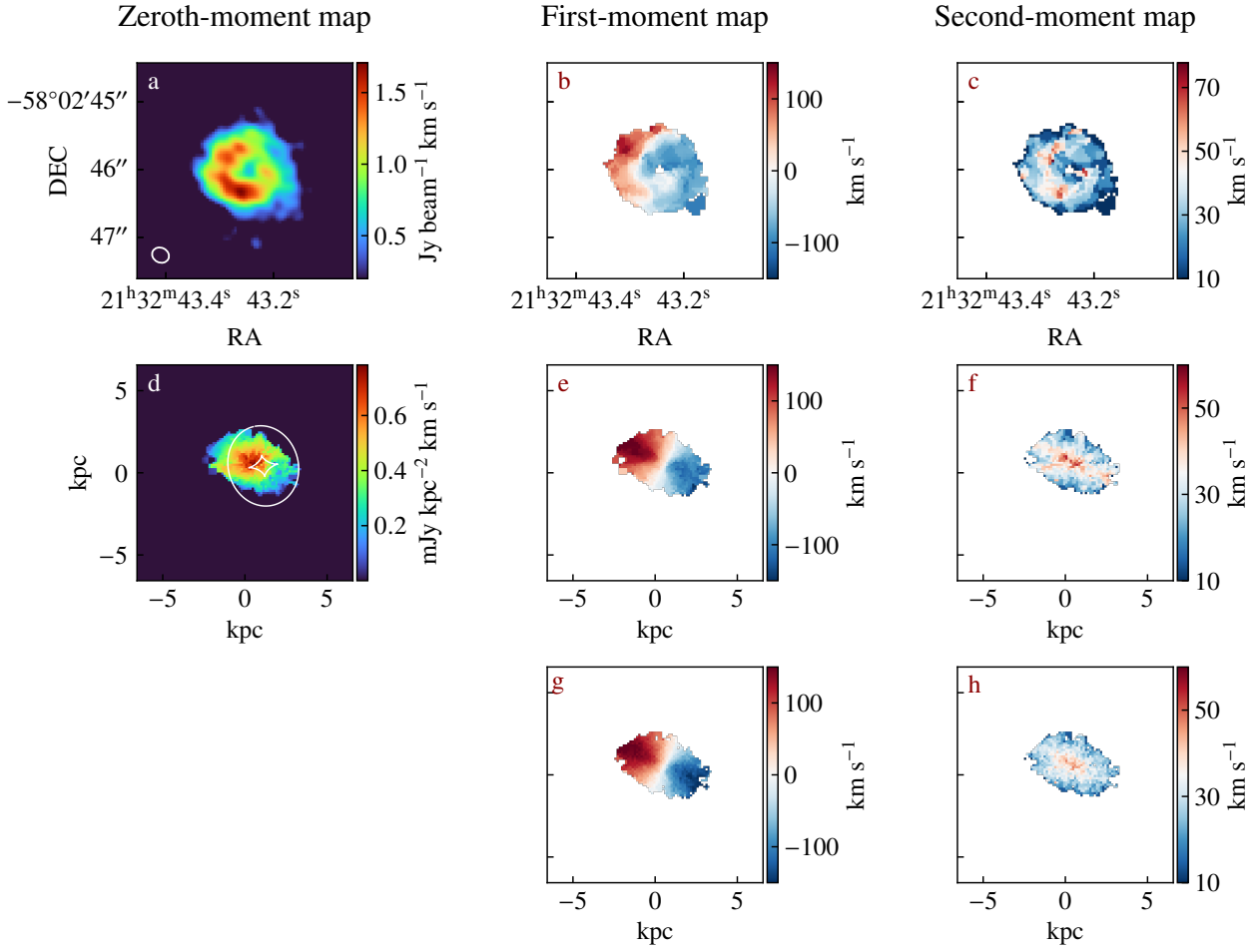


Figure B4. Moment maps for SPT2132-58. Same as in Fig. 1. The beam size, shown as a white ellipse on the lower left corner of panel a, is 0.25×0.22 arcsec² at a position angle of 63.3° .

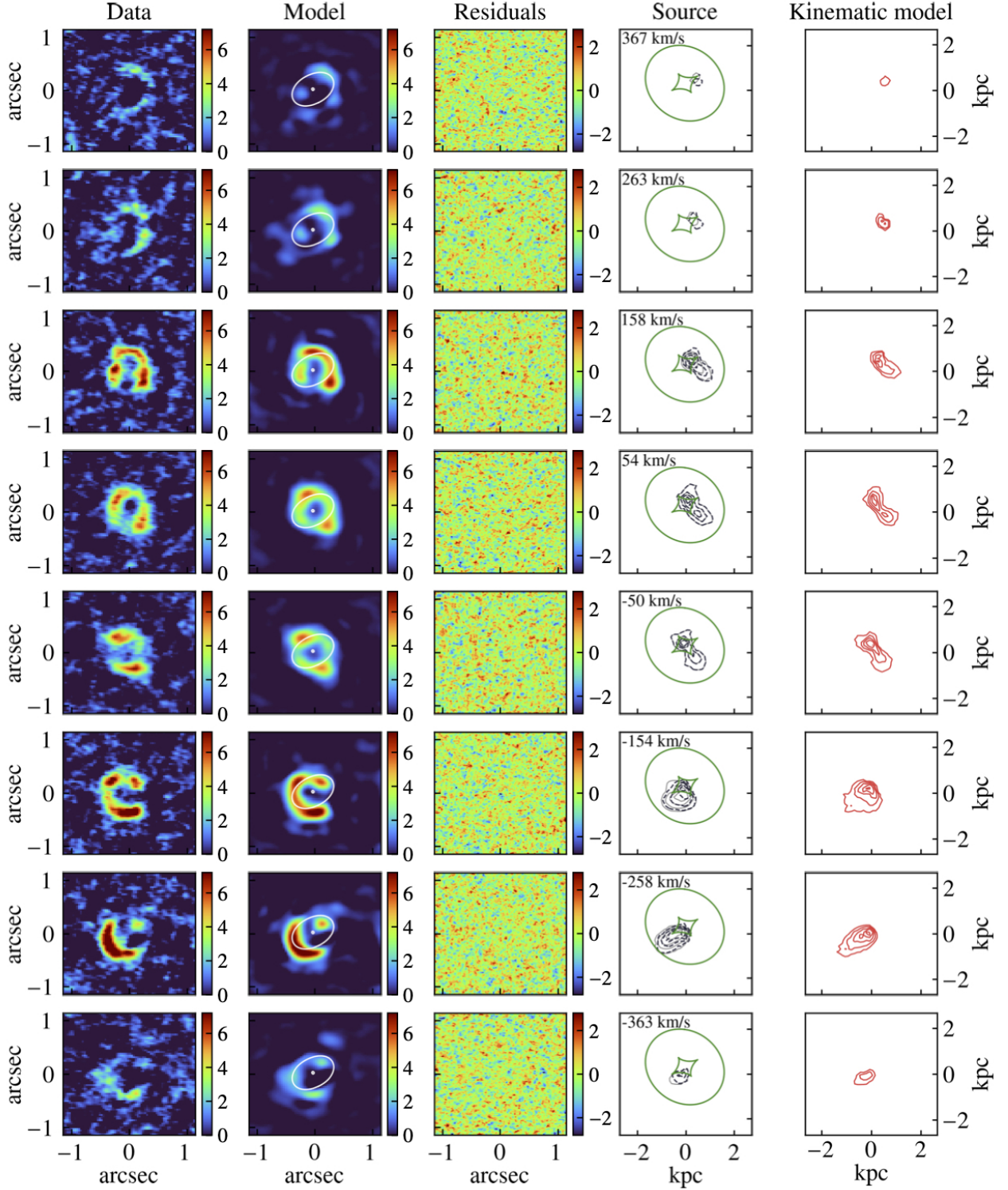


Figure B5. Channel maps for SPT0345-47. Same as in Fig. 2.

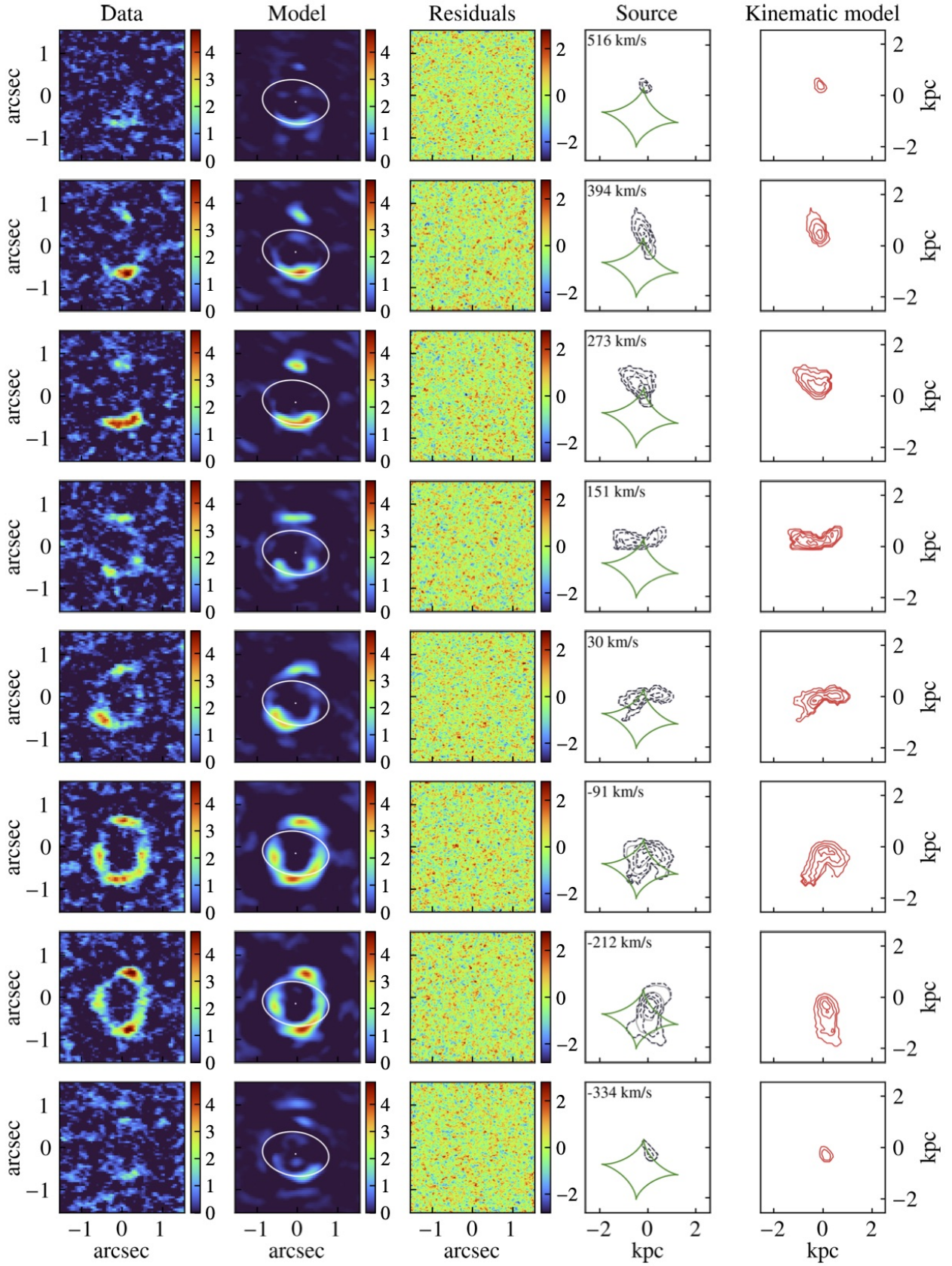


Figure B6. Channel maps for SPT0441-46. Same as in Fig. 2.

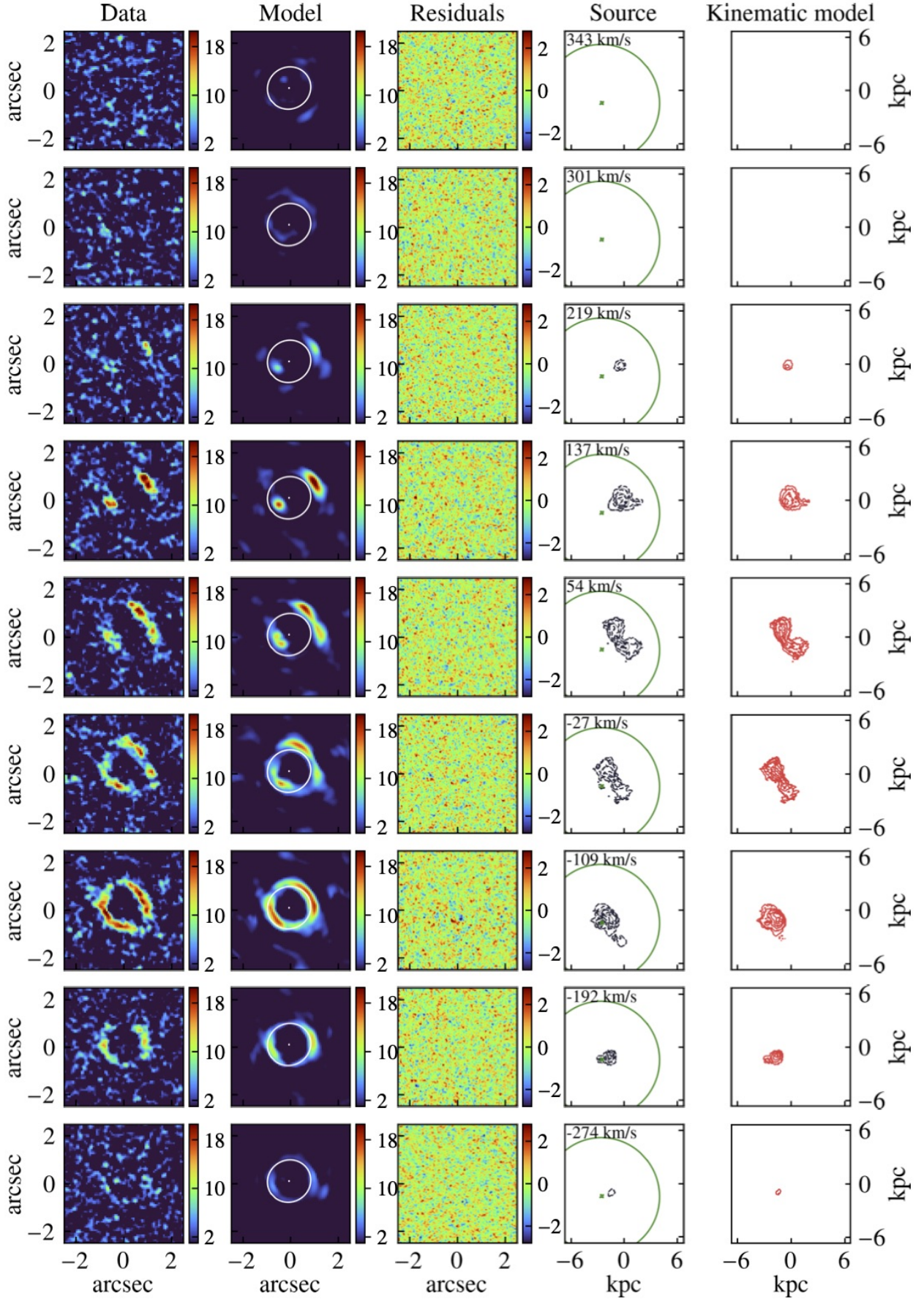


Figure B7. Channel maps for SPT2146-55. Same as in Fig. 2.

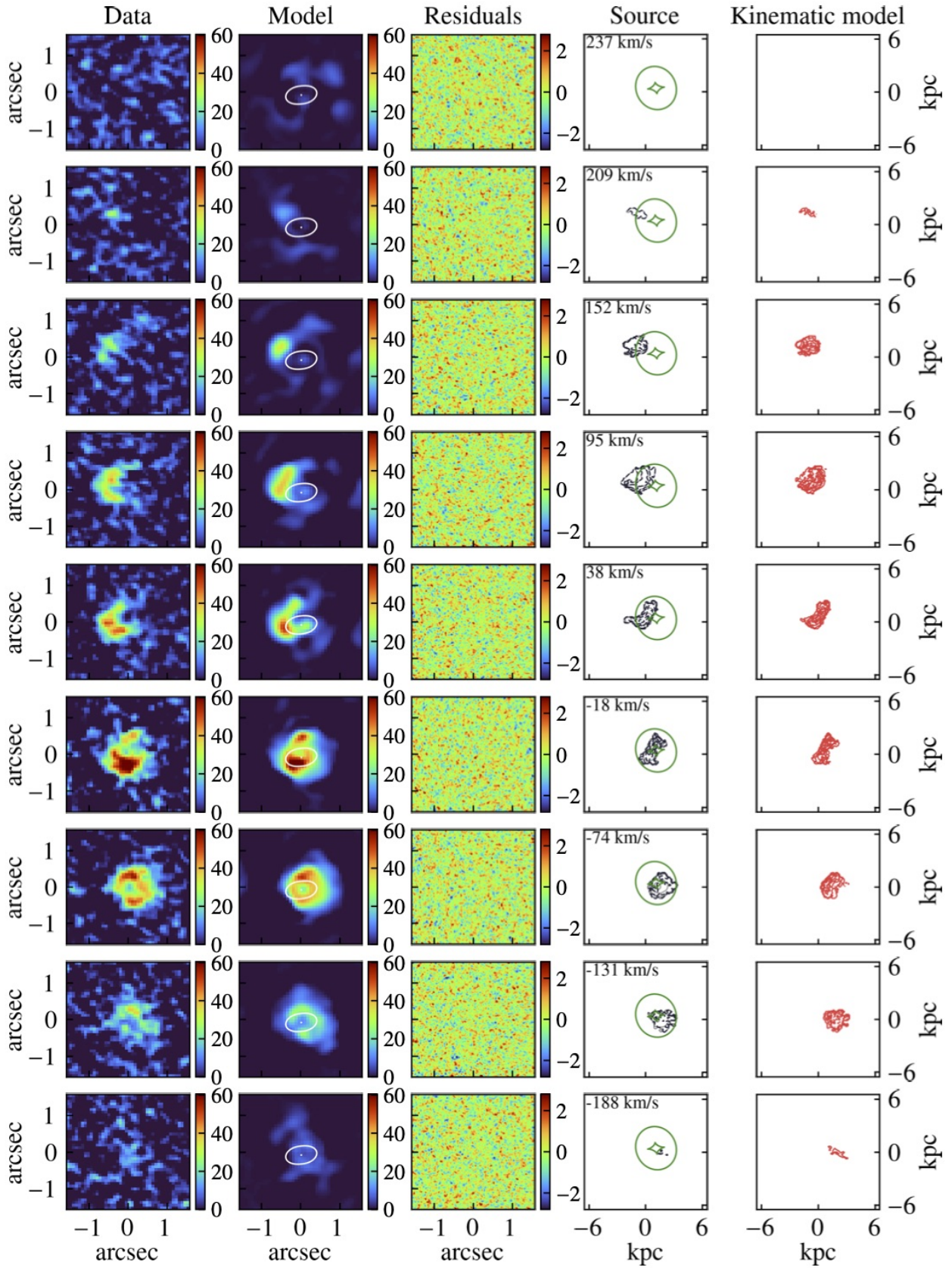


Figure B8. Channel maps for SPT2132-58. Same as in Fig. 2.

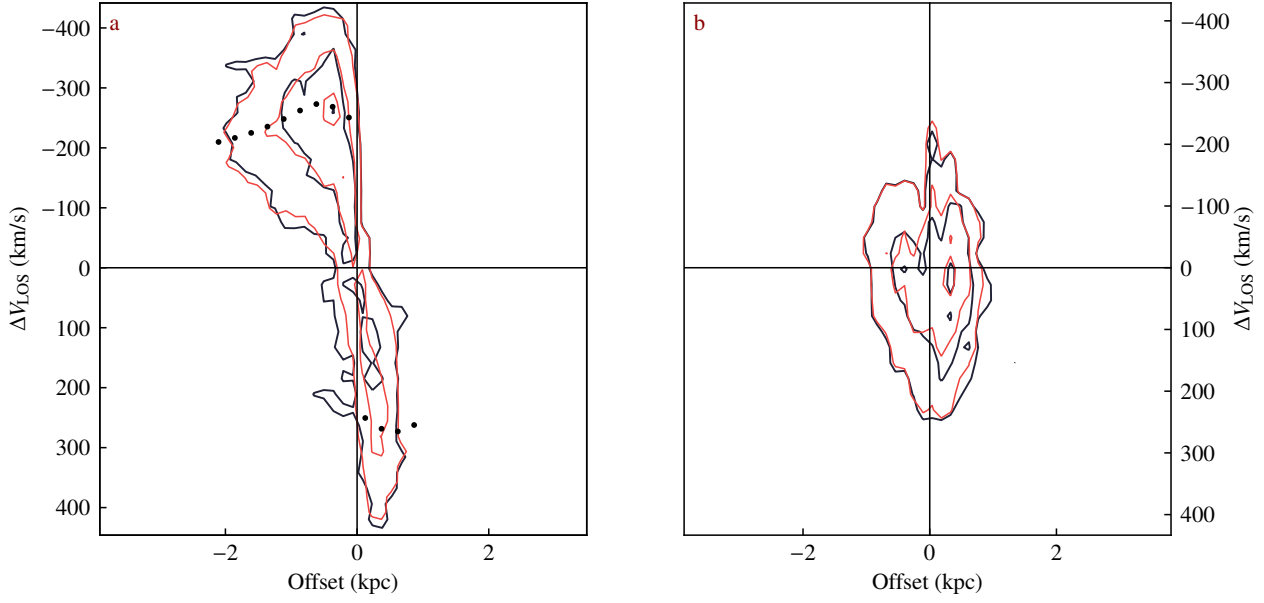


Figure B9. Position-velocity diagrams for SPT0345-47. Same as in Fig. 3.

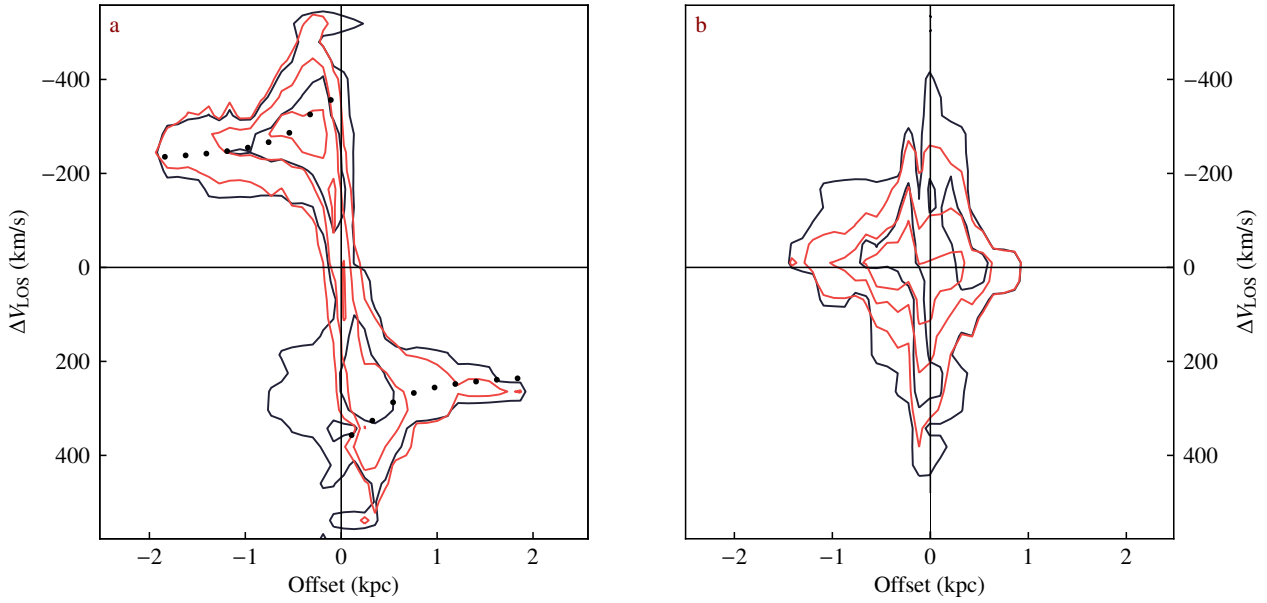


Figure B10. Position-velocity diagrams for SPT0441-46. Same as in Fig. 3.

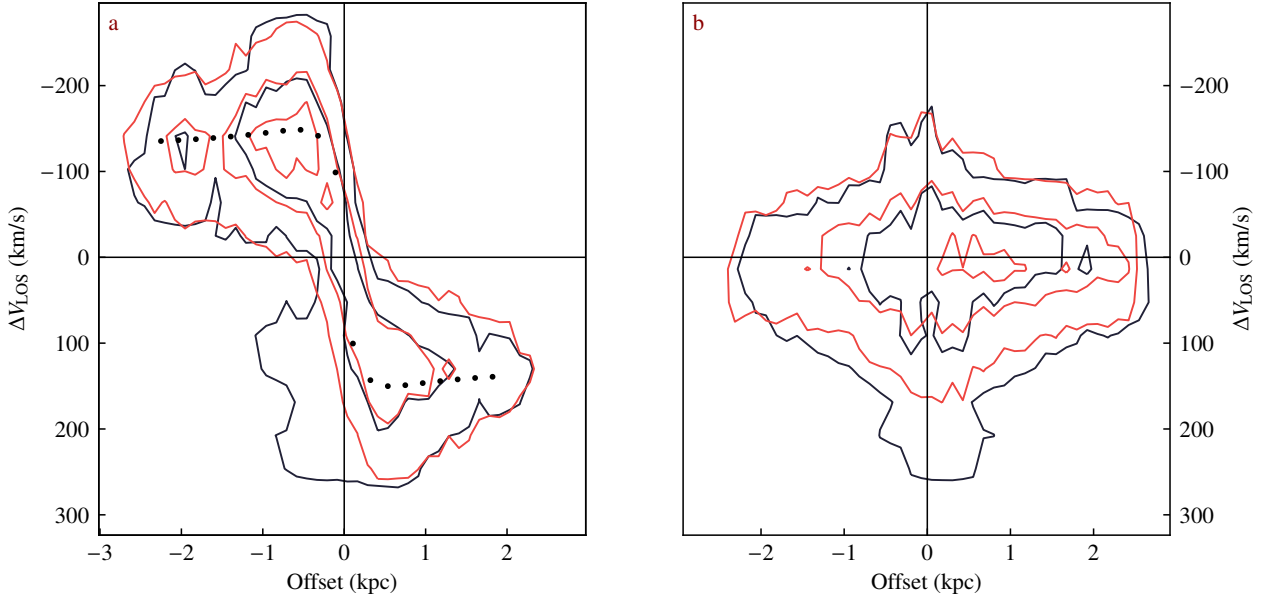


Figure B11. Position-velocity diagrams for SPT2146-55. Same as in Fig. 3.

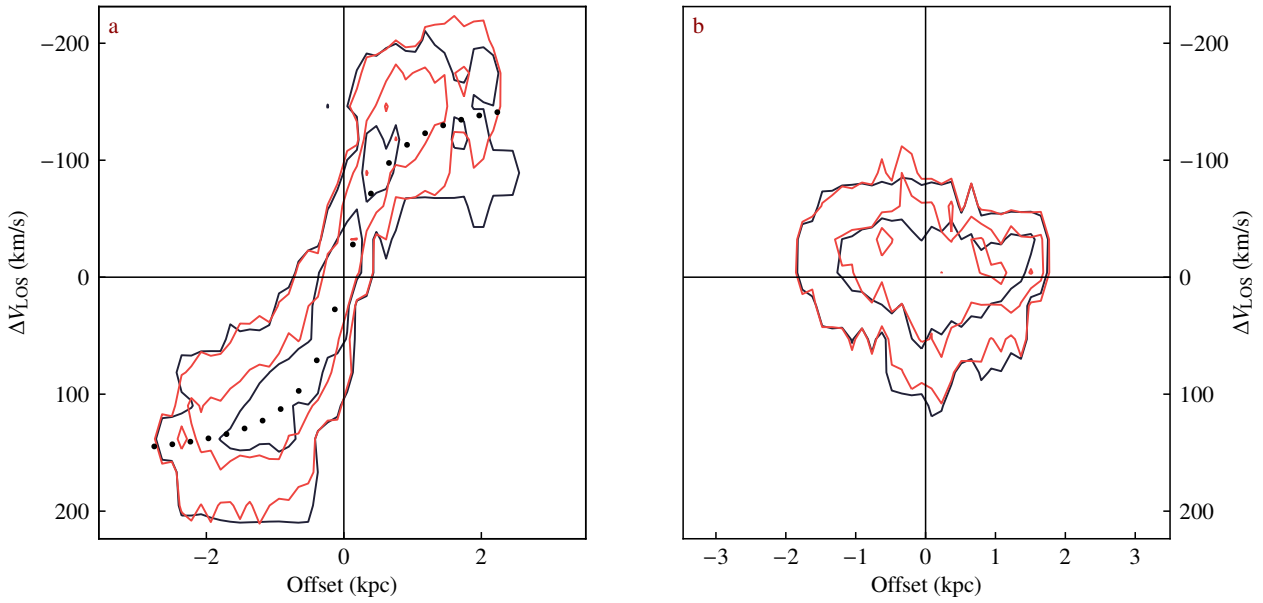


Figure B12. Position-velocity diagrams for SPT2132-58. Same as in Fig. 3.

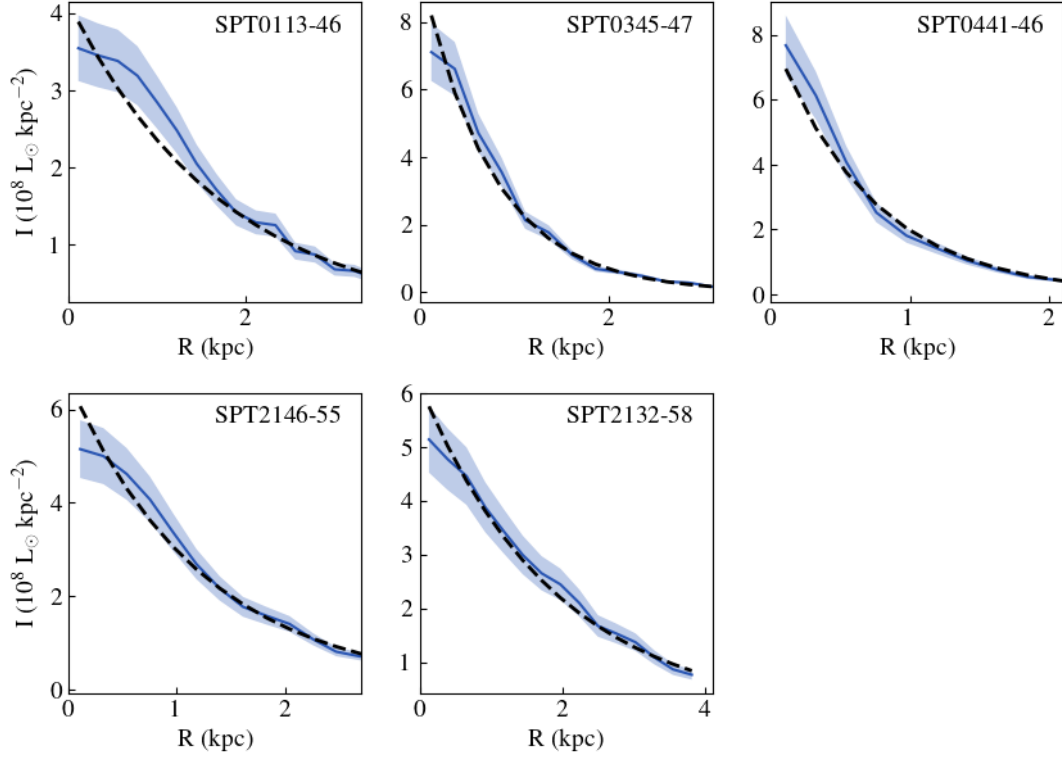


Figure C1. The blue solid lines and the shaded areas show the [CII] profiles and the corresponding uncertainties. These profiles are obtained dividing the zeroth-moment map of the reconstructed sources into rings (with centers, PA and i defined by the values of the kinematic model, Table 3) and calculating the surface densities at a certain radius as azimuthal averages inside that ring. The black dashed lines show the best-fit exponential profiles.

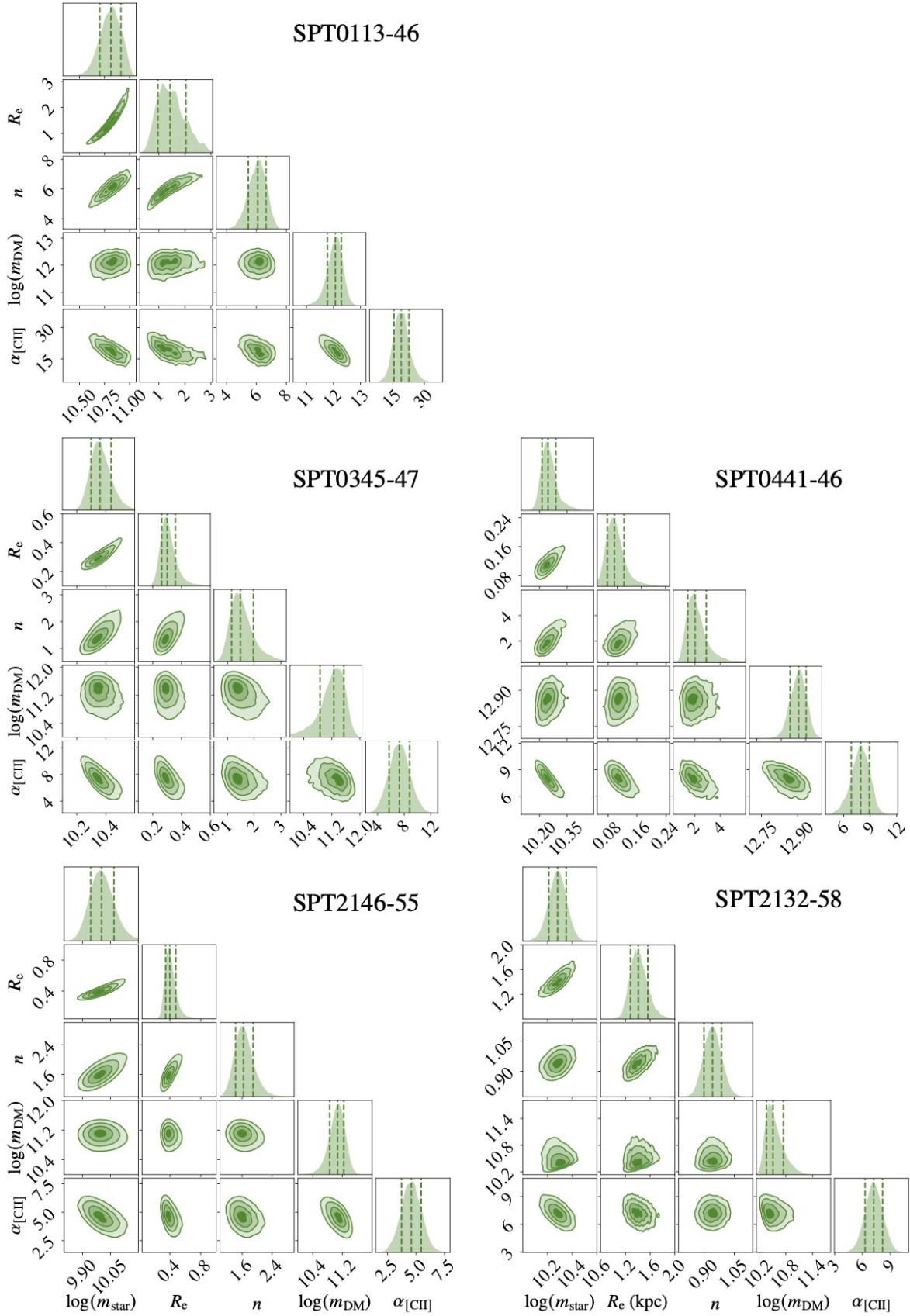


Figure C2. Posterior distributions of the dynamical parameters for the five galaxies studied in this paper, as indicated in the legend. The dashed lines in the 1D histograms show the 16th, 50th and 84th percentiles (see Table 4). In each panel $m_{\text{star}} = M_{\text{star}}/M_{\odot}$ and $m_{\text{DM}} = M_{\text{DM}}/M_{\odot}$. The units of R_e and α_{CII} are kpc and M_{\odot}/L_{\odot} , respectively.